Position Reconstruction with a SiPM Array in Xenoscope, a Vertical DARWIN Demonstrator

---

Master Thesis

Professors:
Prof. Dr. Laura Baudis
Prof. Dr. Paolo Crivelli

Supervision:
Dr. Marta Babicz
Mariana Rajado Silva

Student:
Sana Ouahada

Date: August 28, 2023

Abstract

This master thesis is conducted within the DARWIN project, a next-generation detector for direct dark matter detection utilising a dual-phase xenon Time Projection Chamber (TPC). The experiment represents the ultimate phase to the existing line of XENON detectors at Gran Sasso National Laboratory (LNGS), Italy.

When Weakly Interacting Massive Particles (WIMPs) interact with the liquid xenon target, they generate scintillation and ionisation signals. While the current XENONnT detector employs Photomultiplier Tubes (PMTs) for signal detection, recent advancements in silicon-based photosensors, specifically Silicon Photomultipliers (SiPMs), present promising alternatives for the forthcoming DARWIN experiment.

This thesis focuses on modeling the response of SiPMs within the Xenoscope detector, a vertical demonstrator for DARWIN. By characterizing the SiPM array and simulating electron transport, we explore $x - y$ position reconstruction using a center of gravity algorithm. Disparities in reconstruction bias based on initial positions and interaction energies are observed, with higher accuracy noted for a closer proximity of the source to the photodetectors, varying from $\Delta r = 0.6$ mm for a source placed at ground level to $\Delta r = 0.2$ mm when the source is placed 60 cm away from the photosensor array. Additionally, the analysis highlights the pronounced correlation between source energy and improved reconstruction accuracy with a decrease of 81% when the number of electrons in the interaction is multiplied by a factor 20. This effect proves the significance of selecting high-energy sources for precise reconstructions. The reconstruction accuracy is also observed to be higher within the centers of the photodetectors and diminishes toward the edges of the detector. These effects, aligned with physical consistency, are also attributed to the Centre of Gravity (CoG) algorithmic construction.

Acknowledgements

I would like to express my sincere gratitude to Prof. Laura Baudis, whose guidance and expertise were invaluable throughout my work. I am grateful for the opportunity to work on the Xenoscope project under her supervision at the University of Zurich. A special thanks to Dr. Marta Babicz and Mariana Rajado Silva for their support during the lab work phase, as well as their assistance in thesis writing. I would like to thank Dr. Ricardo Peres for his patience and consistent presence in making the project a success. I also want to acknowledge and appreciate Dr. Michelle Galloway's indispensable expertise and her willingness to share her valuable insights. I am grateful for the overall support from the entire group during challenging moments. Thanks to Prof. Paolo Crivelli at ETH Zurich for agreeing to be my official supervisor and for his continuous involvement in my thesis. Lastly, heartfelt thanks to my family and friends for their constant support throughout my academic journey.

Contents

1 Introduction

In the vast cosmic puzzle, the enigmatic presence of dark matter defies conventional comprehension. Its existence, first postulated by the astute Swiss-American astronomer Fritz Zwicky nearly a century ago, has since been one of the main questions in the field of astrophysics [1].

Over the years, our understanding of dark matter led to the development of cosmic models, suggesting that around 26% of the Universe's composition comprises this unknown form of matter [2]. However, direct evidence of dark matter has not been found to this day and its composition remains a unknown. In response to this cosmic puzzle, a diverse range of experiments has taken root in this search, with the most promising among them employing dual-phase time projection chambers (TPCs). Among these, the DARWIN project emerges as the next-generation experiment, aiming to scale up the current technologies. With a liquid xenon target of 40 tonnes, the project seeks to probe the accessible parameter space for the discovery of weakly interacting massive particles (WIMPs), charting a course to investigate masses above 5 GeV/c^2 [3]. Notably, DARWIN's unprecedented scale and ultra low background give the opportunity to investigate other physics channels, such as the search for neutrinoless double beta decay and measure the solar neutrino flux.

However, these ambitions are accompanied by various technological challenges that must be overcome to navigate the complexities of such experiments. In this context, Xenoscope, a full-scale vertical demonstrator for the DARWIN project, was meticulously constructed at the University of Zurich. This endeavour carries the critical mission of testing the feasibility of electron drift over a distance of 2.6 metres within a dual-phase xenon TPC [4]. This work, in particular, delves into a crucial facet of the Xenoscope project: choosing the optimal photosensors, which play an indispensable role in the success of this pioneering research effort.

2 Dark Matter Research

2.1 Dark Matter Evidence

Only 5% of the Universe's total mass-energy is composed of ordinary matter. In contrast, the quantity of dark matter is roughly estimated to surpass that of ordinary matter by more than 5 times. As seen in Figure 1, the remaining majority is attributed to dark energy, responsible for the accelerating expansion of the Universe [5]. In 1933, the astronomer F. Zwicky inferred the concept of Dark Matter when he investigated the velocity distribution of galaxies within the Coma Cluster [1] . His exploration of galactic dynamics within the Coma cluster led to the recognition of anomalies, revealing a mismatch between the observed mass of the Cluster and the predicted values from the virial theorem [6].

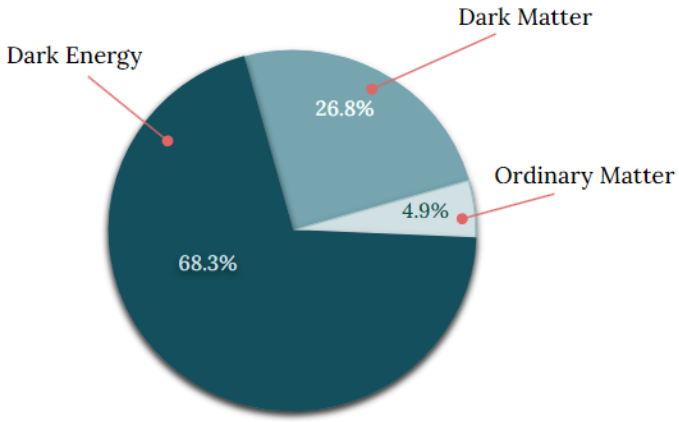

Figure 1: The energy-matter composition of the Universe, deduced from models of temperature fluctuations in the Cosmic Microwave Background (CMB). CMB refers to the residual radiation from the Big Bang. It is instrumental in explaining evidence for dark matter. Temperature fluctuations in the CMB arise due to the gravitational effects of dark matter on the distribution of matter in the early universe. Numbers from [7].

Several decades later, groundbreaking observations by Vera Rubin and Kent Ford [8] showed that the orbital velocities of outer regions of galaxies do not follow a velocity model derived from the classical theory of gravitation. There is a discrepancy between observed galactic rotational curves and the prediction based on Newtonian mechanics. From the predictions, the rotational speed of stars, $v(r)$ at the distance r from the galaxy centre which matter distribution are given by $M(r)$ is:

$$v(r) = \sqrt{\frac{GM(r)}{r}}, \tag{2.1}$$

where G is the gravitational constant and $M(r)$ is the mass enclosed by the orbit. Their observations revealed a nearly constant value forming a flat rotation curve instead of decreasing with the distance r. A possible interpretation would be the existence of a spherical dark matter halo with a density profile of $\rho(r) = 1/r^2$ [8]. Subsequent to this discovery, a series of observations followed, including for example the study of the NGC 6503 galaxy. The study of the velocity dispersion in this galaxy illustrates precisely the phenomenon described—a notable mismatch between the observed velocity data points and the predictive models reliant solely on visible matter.

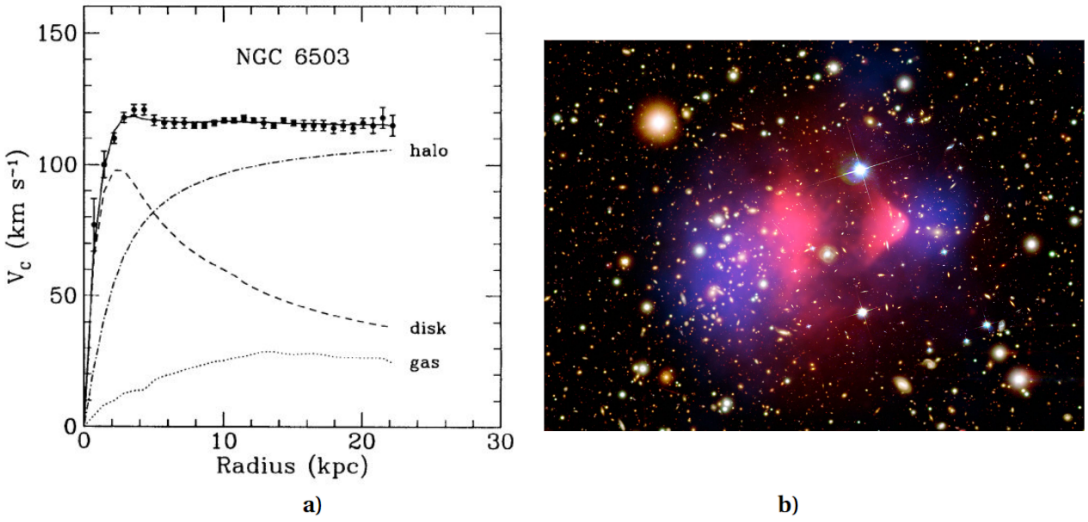

Figure 2: a) The galactic rotation curve of the NGC 6503 spiral galaxy illustrates the relationship between the rotation velocity (V_c) and the distance to the center of the galaxy. The observed data points from NGC 6053 gas does not align with the predicted contribution from luminous matter (disk). Conversely, the dark matter halo's anticipated effect (dashed-dotted line) corresponds more closely to the measured data. The collective influence of all three contributions - luminous matter, gas, and dark matter - offers a fitting representation of the data. This alignment underscores that the composition of the galaxy extends beyond visible matter, indicating the presence of a significant dark matter component [9]. **b)** The "Bullet Cluster" displays a collision between two galaxy clusters. The noticeable separation between most of the matter shown in the clusters and baryonic matter distributions provides clear evidence of dark matter[10].

Another compelling piece of evidence supporting the observation of dark matter comes from the exploration of galaxy cluster collisions. This phenomenon unveils gravitational interactions that cannot be solely attributed to visible matter.

In the composite image depicted in Figure 2, galaxies and stars are represented in orange and white, captured by the Magellan and Hubble Space Telescopes. The pink distributions indicate X-ray-emitting hot gas, detected by the Chandra X-Ray Observatory, containing the majority of ordinary matter. The blue areas in the image show the distribution of non-luminous mass within the clusters [11]. This mapping results from gravitational lensing, a phenomenon where massive objects deflect light from more distant ones because of their gravitational fields. The goal is to find the distribution of mass in regions where direct observation might be limited, providing in this situation insights into the existence and characteristics of dark matter. An intriguing observation arises from the visible deceleration of the hot gas during the merger of the clusters, attributed to a drag force. However, the mass indicated by gravitational lensing was not subjected to such deceleration during this process. This discrepancy suggests a form of matter that interacts primarily through gravity and very weakly with itself or the gas. When the clusters collided, the clumps of dark matter advanced ahead of the hot gas, leading to the visual separation between dark and normal matter in the image. This separation would not occur if hot gas were the heaviest constituent of the clusters, as proposed by modified gravity theories [12]. Instead, this discovery lends support to the existence of dark matter.

2.2 Dark Matter Candidate

While the presence of dark matter is well-established, its exact nature remains a mystery. On the side of particle dark matter, a diverse array of properties for potential candidates emerges from cosmological and astrophysical observations. These candidates possess a set of defining attributes, including:

- **Gravitational Interaction:** Dark matter candidates are expected to interact primarily through gravity, a phenomenon that contributes significantly to the formation and behaviour of cosmic structures.

- **Neutral and Non-Electromagnetic:** Potential candidates exhibit extremely small electromagnetic interactions, such as light absorption, emission, or reflection. There is, to this date, no observed evidence of their potential decay into charged particle pairs or photons.

- **Non-Baryonic Nature:** Insights from CMB data indicate that dark matter is distinct from ordinary baryonic matter. Baryonic matter consists of protons and neutrons, which are made up of quarks, participating in strong and electromagnetic interactions. Dark matter is believed to be composed of particles fundamentally different from the particles making up atoms.

- **Non-Relativistic at Decoupling:** Dark matter candidates must become non-relativistic during decoupling from the thermal bath, marking the phase when their interactions with radiation decrease. This transition, where dark matter moves at speeds much lower than the speed of light, plays a crucial role in shaping the formation of large-scale structures in the Universe [13].

- **Stability or Long Lifetime:** Their stability, or alternatively, a sufficiently long lifetime, is implied by their early thermal production in the Universe. This trait is essential for explaining their presence from the early Universe to the present day.

These criteria serve as guiding principles for identifying plausible candidates and formulating a more comprehensive understanding of the fundamental characteristics of dark matter. Potential candidates for non-baryonic dark matter can first be explored among the particle types that are already familiar within the framework of the Standard Model (SM) [14]. One notable candidate is the neutrino, which was already moving at relativistic speeds during the decoupling era. However, neutrinos would represent a "hot" type of dark matter and are unable to explain the observed formation of large-scale structures in the universe. While studies involving both the characteristics of these large structures and CMB observations do indicate a physical density of neutrinos, this density falls short of accounting for the predicted abundance of dark matter [15].

Therefore, the range of potential candidates for dark matter in ongoing research extends beyond the Standard Model of particle physics. Among these candidates, a prominent contender is the Weakly Interacting Massive Particle (WIMP). This model is currently favored because WIMPs are considered as "cold" dark matter candidates, had relatively low speeds at the time of decoupling. This characteristic enabled them to play a crucial role in the formation of the large-scale structures observed in the Universe. This particle arises from a supersymmetric extension of the Standard Model (SUSY), a theoretical framework that aims to reconcile some of the existing gaps in our understanding of fundamental particles and their interactions [16]. This category of particles could have masses spanning from approximately 1 GeV/c^2 to 100 TeV/c^2, and would interact with Standard Model particles on the weak scale. The reason for WIMPs being the leading candidate currently rests on the hypothesis of the "WIMP miracle" or the freeze-out hypothesis according to which dark matter is a thermal relic of the early universe [17]. Essentially, the observed abundance of dark matter in the Universe can be explained by the notion that WIMPs were once in thermal equilibrium with other particles in the early Universe. They subsequently decoupled and "froze out", leaving behind the amount of dark matter we observe today. In cosmological models, a simplification is employed where, in the early Universe, all particles are considered to be relativistic and in a state of thermal equilibrium. As the Universe cools down, some particles decouple and their number density reduces rapidly.

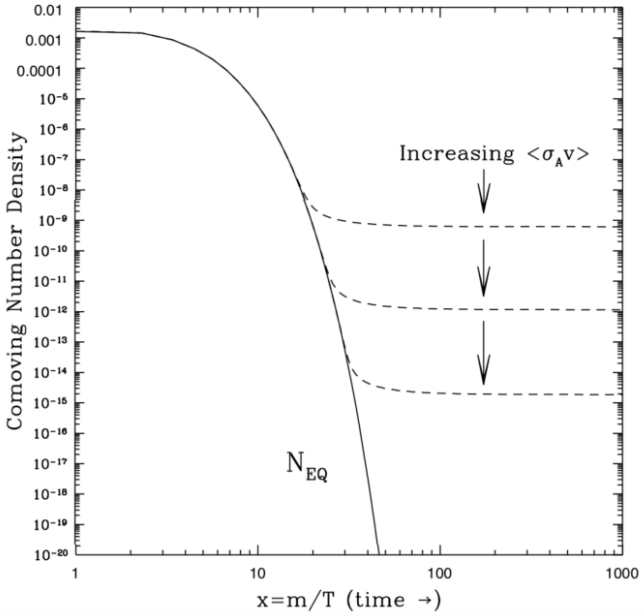

Figure 3: Comoving WIMP number density over time. The solid lines represent the equilibrium state and the dashed lines show the relic abundance of WIMP particles, i.e their current quantity remaining from the Big Bang. The x-axis, represented as (m/T), quantifies the ratio between the WIMP mass (m) and the temperature (T), which is directly since the Big Bang. The relic abundance depends on the the WIMP velocity v and the annihilation cross section σ_A. As the product of these 2 quantities increases, the number of WIMPs remaining after freeze-out decreases [18].

If we solely account for the process described, the density of dark matter would gradually decrease until it eventually disappears entirely. Nonetheless, the expansion of the universe plays a crucial role; as it expands, dark matter particles become increasingly sparse, causing their likelihood of interaction to progressively decline. This process, known as freeze-out, results in the number of dark matter particles approaching their relic density in an asymptotic manner. This phenomenon is illustrated over time or as a function of the temperature of the Universe in Figure 3. It shows the change in dark matter density as a function of the temperature of the Universe, illustrating how the freeze-out process gradually approaches the relic density.

2.3 Dark matter Detection

2.3.1 Types of Detection Experiments

There are three main detection techniques used nowadays in dark matter searches as schematically represented in Figure 4.

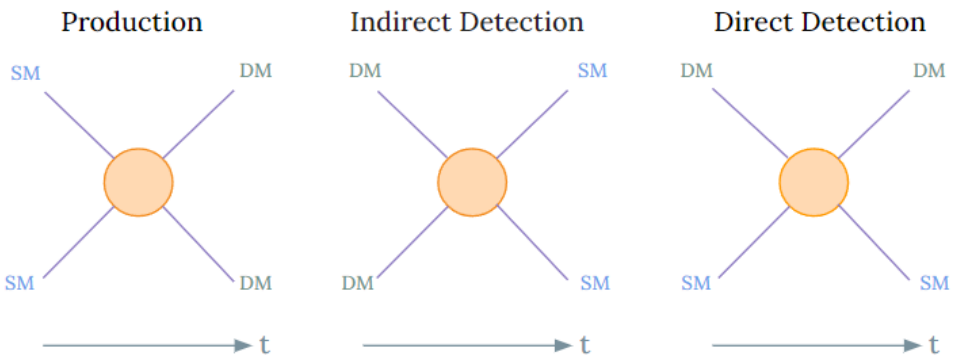

Figure 4: Illustration of approaches for detecting dark matter. Production searches try to generate dark matter particles through high-energy collisions involving SM particles, with missing energy as the signature of the production. Indirect search strategies focus on detecting SM decay products of dark matter annihilation. Lastly, the direct detection of dark matter aims to detect dark matter particles colliding with Standard Model particles.

One of the efforts for dark matter searches resides in the production process. Generating dark matter particles in particle colliders results in a distinct signature: the absence of energy and transverse momentum. This occurs as the particles do not get detected, leaving behind no trace. Numerous efforts have been dedicated to production searches, including those undertaken by experiments like ATLAS (A Toroidal LHC Apparatus) and CMS (Compact Muon Solenoid) at the LHC (Large Hadron Collider) [19].

Indirect detection of dark matter encompasses the quest for SM particles produced as a result of the annihilation of dark matter particles. Typically, these searches focus on areas where WIMP dark matter is anticipated to be most densely distributed: the cores of galaxies and galaxy clusters. Several ground-based experiments contribute to this pursuit, among them: HESS (High Energy Stereoscopic System) [20], VERITAS (Very Energetic Radiation Imaging Telescope Array System) [21] and MAGIC (Major Atmospheric Gamma Imaging Cherenkov) [22].

Finally, another channel to detect dark matter particles is direct detection. In order to observe the weakly interacting particles collide with nuclei in some target medium, the search must be conducted using highly sensitive low-background experiments. These interactions can potentially occur with the atomic nuclei within the target material or with their surrounding electron clouds. Due to the neutral property of WIMPs, the primary interaction of interest centres around elastic scattering with the atomic nucleus itself. This leads to the occurrence of a nuclear recoil (NR) [23].

2.3.2 Current Experiments

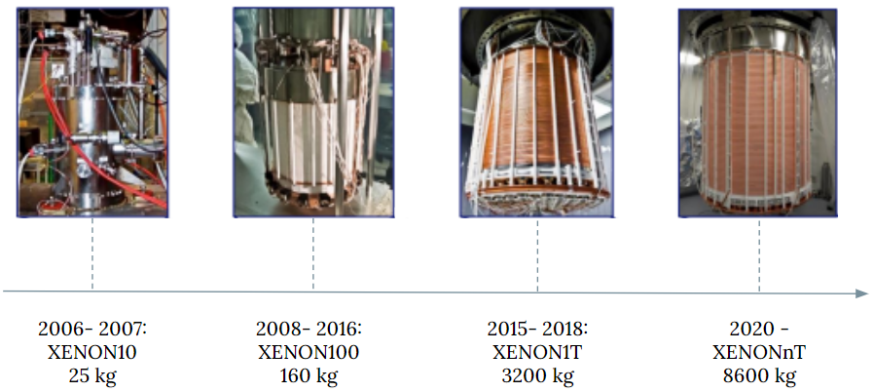

Figure 5: The evolution of the XENON project's timeline and the corresponding total xenon mass employed in each XENON detector is outlined [24].

A wide array of direct detection experiments exists, employing diverse target materials and detection techniques. A common requirement among these experiments is the pursuit of minimal backgrounds and low energy thresholds, which are crucial for detecting rare, low-energy recoils. The conventional strategy entails shielding with high-density, low-radioactivity substances, complemented by water shields [25]. To counter cosmic radiation, installations are strategically located in deep underground laboratories, intercepting the cosmic-ray radiation influx.

Within this direct detection method, three primary channels exist [25]. The first is scintillation, where the target material emits photons upon receiving energy from an incoming particle. Mechanical energy transfer also occurs as heat or phonons in crystalline structures. Ionisation, the release of electrons from the target, forms the final detection avenue. Experiments harness one or more of these methods, often through multi-channel readout. This facilitates the differentiation of NRs and electronic recoils (ERs), offering a potent mechanism for background rejection.

In nuclear recoils involving the interaction between WIMPs and atoms in the target material, typically two types of interactions are taken into account: spin-independent (SI) and spin-dependent (SD) interactions. These interactions contribute to the total cross-section and can be categorised into two distinct factors contributing to the cross-section $\frac{\mathrm{d}\sigma}{\mathrm{d}E_{\mathrm{NR}}}$:

$$\frac{\mathrm{d}\sigma}{\mathrm{d}E_{\mathrm{NR}}} = \alpha\sigma_0^{\mathrm{SI}} + \beta\sigma_0^{\mathrm{SD}}, \tag{2.2}$$

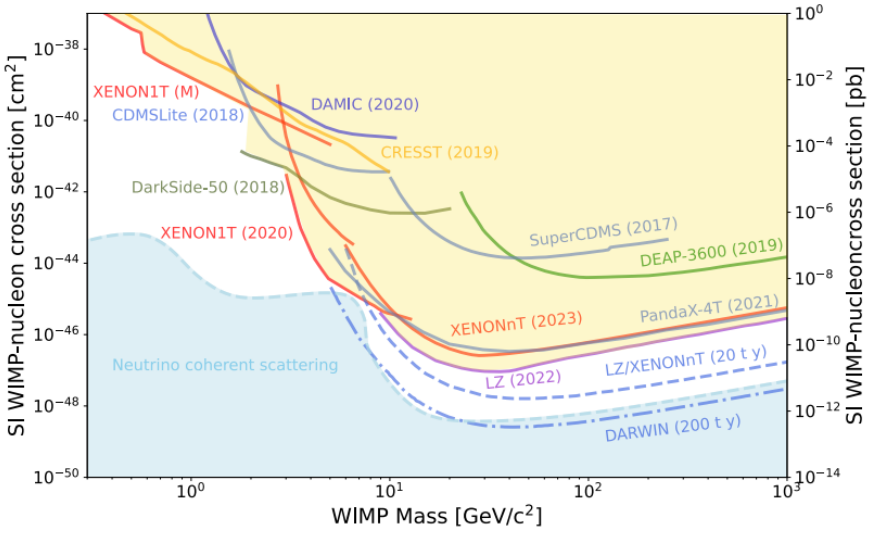

Figure 6: WIMP-nucleon spin-independent cross section limits (solid lines) from current dark matter experiments and projections (dashed) for planned direct detection dark matter experiments. The yellow area illustrates the extent to which these experiments can exclude certain interaction strengths. The blue region outlines the neutrino floor, representing a theoretical lower threshold for detecting WIMP-like dark matter in direct detection experiments. Neutrino discrimination is crucial as they are expected to have similar interaction characteristics with matter, making their distinction challenging with potential dark matter particules. This concept often signifies the point where dark matter signals become indistinguishable from a background created by neutrinos, which have very similar characteristics [26].

where α and β depend on the respective nuclear form factors. Figure 6 illustrates the latest understanding of the WIMP-nucleon spin-independent cross-section. This structure lets us compare experiments that use different target atoms. This comparison includes various WIMP masses and WIMP-nucleon cross sections. When there are no observed events, specific parts of the parameter space can be ruled out. This is usually done with a 90% confidence level. Based on this plot, the current leaders in direct dark matter searches with highly effective exclusion limits are the dual-phase noble gas Time Projection Chambers (TPCs). These experiments stand out due to their capacity to simultaneously measure scintillation light and ionisation charge, thereby positioning them at the forefront of groundbreaking advancements. Measuring both scintillation light and ionisation charge allows for discrimination between NRs and ERs, crucial for background rejection. In particular, the upcoming searches led by DARWIN aim to reach the lower limit defined by background originating from neutrino emissions from the Sun, the atmosphere, and the diffuse supernovae background.

3 DARWIN and its Vertical Demonstrator

3.1 Noble Gas Dual-phase Time Projection Chambers

3.1.1 Xenon as a Detection Medium

The exclusion diagram depicted in Figure 6 underscores the potential of noble gas dual-phase TPCs as valuable detectors for elevating the sensitivity of direct WIMP searches. Prominent experiments in this category, such as those in the XENON, LZ and PandaX initiatives [27, 28, 29], have notably leveraged xenon as the primary detection medium within their target volumes. In all of these detectors, most of the volume is occupied by the liquid phase of xenon, acting as the target material; and a small gas phase is situated on top.

Among noble elements, xenon stands out due to its strong ability to produce both high charge and light output for nuclear reactions – the signals expected from WIMP-nucleon interactions. This makes Liquid Xenon (LXe) an excellent candidate for WIMP detection. Furthermore, its capacity to be easily scaled up for larger detectors is a clear advantage. The dense nature of liquid xenon (density: 3 g/cm^3) offers effective self-shielding and a compact detector design. With its high atomic mass of $A \approx 131$, xenon is a suitable choice as it increases the spin-independent cross section, proportional to A^2. Additionally, the absence of long-lived radioactive isotopes guarantees the attainment of an ultra-low background level [30]. One of the leading experiments in the field is the line of XENON projects, whose timeline is represented in Figure 5.

When a WIMP interacts with a xenon atom, the energy transfer occurs through ionisation, excitation, and heat distribution. Scintillation light can be generated through two distinct mechanisms. The xenon atom that undergoes recoil becomes excited, combines with another atom, forming an excited diatomic molecule [31]. During its subsequent de-excitation, it emits a photon with a wavelength of 178 nm in the vacuum ultra-violet (VUV) range [32]. This phenomenon is described by the following equations:

$$\mathrm{Xe}^* + 2\mathrm{Xe} \rightarrow \mathrm{Xe}_2^* + \mathrm{Xe} \tag{3.1}$$

$$\mathrm{Xe}_2^* \rightarrow 2\mathrm{Xe} + h\nu. \tag{3.2}$$

Electron-ion pairs resulting from ionisation can undergo recombination, leading to the creation of excited states. When no electric field is applied, or if the field's strength is insufficient to fully separate all ion-electron pairs, a portion of xenon ions Xe^+ will engage in recombination. This recombination process results in additional scintillation light originating from xenon dimers. The process unfolds as follows:

$$\begin{aligned} Xe^+ + Xe &\rightarrow Xe_2^+ \\ Xe_2^+ + e^- &\rightarrow Xe^{**} + Xe \\ Xe^{**} &\rightarrow Xe^* + \text{heat} \\ Xe^* + Xe &\rightarrow Xe_2^* \\ Xe_2^* &\rightarrow 2Xe + h\nu. \end{aligned} \tag{3.3}$$

The total number of scintillation photons produced by an interaction is therefore given by:

$$N_{\text{photons}} = a.N_{ex} + b \cdot r \cdot N_i, \tag{3.4}$$

where N_{ex} is the number of direct excitons, r is the fraction of ions that recombine dependent on the applied electric field, N_i is the number of ions and a, b are the coefficients representing the efficiencies to produce the photons [33]. The number of produced electrons would then be:

$$N_e = b \cdot (1 - r) \cdot N_i. \tag{3.5}$$

The energy released in the interaction can be written as:

$$E = W \cdot (N_{\text{photons}} + N_e). \tag{3.6}$$

Due to different ionisation processes, the ratio between the two values N_{photons} and N_e is different between nuclear and electronic recoil events:

$$\left(\frac{N_e}{N_{\text{photons}}}\right)_{ER} > \left(\frac{N_e}{N_{\text{photons}}}\right)_{NR}, \tag{3.7}$$

which allows for background discrimination [32].

3.1.2 Working Principle of a Xenon Dual-Phase TPC

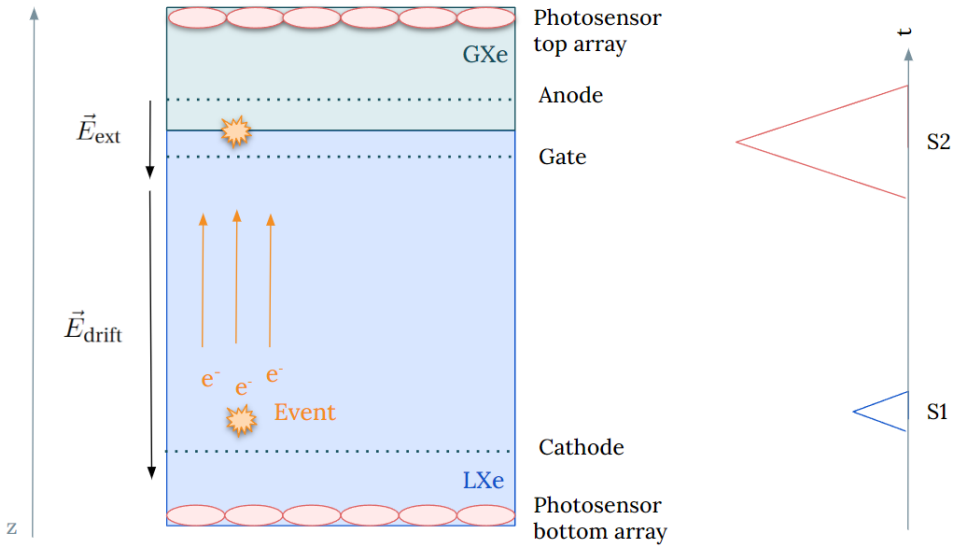

Figure 7: Working principle of a xenon dual-phase TPC. The initial scintillation light emission (S1) generated within the LXe medium is captured by photosensors (mainly the bottom array). After the ionisation electrons drift towards the gate and are extracted into GXe, a delayed secondary light signal, denoted as S2, is produced through proportional scintillation. The drift field ($\vec{E}_{drift}$) and extraction field ($\vec{E}_{ext}$) are also represented.

In the base design of a dual-phase TPC, the target medium is the liquid phase and defines the drift region between the cathode and the gate. On top of the liquid phase is situated a smaller gas phase. As seen on the diagram in Figure 7, there is a liquid-gas interface in the extraction region that is roughly equidistant from both electrodes [34]. When a particle interacts within the LXe target, the energy exchange occurs through scintillation, ionisation, and heat distribution. The immediate emission of scintillation photons at 178 nm is captured by arrays of photosensors, resulting in the S1 signal [25]. Following ionisation, free electrons are guided toward the gate by the vertical electric field, denoted as $\vec{E}_{drift}$. Upon reaching the gate, these electrons are drawn from the liquid to the gas phase due to a stronger applied field between the gate and the anode: the extraction field. This process induces proportional scintillation, generating a delayed scintillation signal called S2.

One of the primary advantages inherent to a dual-phase TPC lies in its ability to reconstruct three-dimensional positions of interactions.

By analysing the shape of the S2 signal captured by the top array of photosensors, the $x - y$ position can be found. This position resolution depends on the geometry and granularity of the photosensor array and its distance to the liquid-gas interface [35]. Determining the $z-$position is achievable through the time delay between the S2 and S1 signals, using the known value of the electric field.

Using its two signals topology, the dual-phase TPC offers the capability for volume fiducialisation through position-based methods. It enables background discrimination using the scintillation signal strength ratio: S2/S1, where typically ER events exhibit a higher electron count compared to NR events. This approach uses xenon's innate self-shielding characteristic, effectively eliminating events originating near the detector walls where there might be elevated background levels [25].

In cases where the extraction field strength is sufficient (around 10 kV/cm), the efficiency of charge extraction from liquid to gas phase is nearly 100%. Dual-phase xenon TPCs have taken a leading role in the direct dark matter search over the past decade. Nonetheless, several challenges remain to be addressed in order to successfully scale up to the DARWIN project and enhance the achievements of the XENON collaboration efforts [27].

3.2 The DARWIN Observatory

DARWIN aspires to enhance the sensitivity of WIMP searches when compared to the presently operational XENONnT experiment. The primary objective is to extend the exploration of cross-section ranges involving WIMPs above a mass of 5 GeV/c². A depiction of DARWIN's foundational design is illustrated in Figure 8.

Achieving these objectives entails expanding the total detector mass to 50 tons, of which 40 tons will constitute the active liquid xenon target. This expansion will coincide with a groundbreaking reduction in background noise. In response to the cosmogenic neutron background, the detector will be positioned within an underground facility, likely the LNGS, bolstered by both a neutron-veto system and a water shield featuring an active Cherenkov veto. For its baseline design, the DARWIN TPC will assume a cylindrical configuration, with dimensions of 2.6 meters in diameter and height. This configuration will be securely encased within a double-walled cryostat. The options for photosensors encompass two choices: Photomultiplier tubes (PMTs) and Silicon photomultipliers (SiPMs), responsible for light detection in both upper and lower arrays. Notably, a hybrid arrangement, such as employing PMTs at the base and SiPMs on top, is under active consideration.

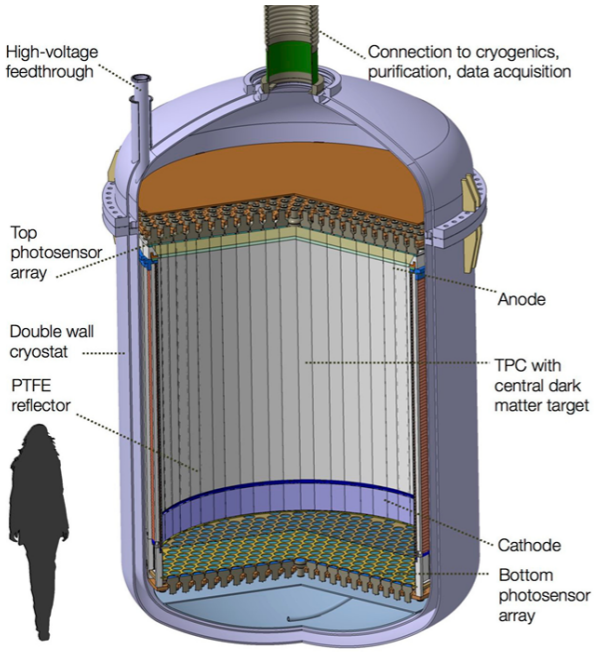

Figure 8: Rendering of the DARWIN TPC baseline design where the main parts of the detector are indicated [3].

Benefitting from its extensive mass, low-energy threshold, and minimal background interference, such a detector holds the potential to detect a range of other rare interactions. Beyond its primary focus, other main searches include identifying solar axions, exploring galactic axion-like particles, and studying the neutrinoless double-beta decay of ^{136}Xe. The detector will also be able to measure the low-energy solar neutrino flux with precision levels exceeding 1%, observe coherent neutrino-nucleus interactions, and even detect the occurrence of galactic supernovae [36, 37]. DARWIN faces various technical challenges to achieve its science objectives. These challenges include in particular background mitigation and scaling issues [24]:

- **Background Mitigation**: XENONnT demonstrated the reduction of intrinsic radiogenic background from ^{222}Rn to less than 1 μBq kg^{-1} using dedicated distillation columns. Achieving DARWIN's stringent background level requires reducing radiogenic background to 0.1 μBq kg^{-1}.

- **Scaling Challenges**:

  – Electrodes: Developing robust electrodes to support the enlarged 2.6 m diameter of the future detector.

- Electron Drift: Adapting electron drift over the unprecedented distance in LXe TPCs, necessitating efficient purification and field cage design.

- Electric-Field Uniformity: Ensuring spatial and temporal field uniformity and preventing charge-up of polytetrafluoroethylen (PTFE) panels.

- High-Voltage (HV) Transfer: Facilitating HV transfer to the cathode, reaching 100 kV.

- Drift Field: A high drift field is vital for improved ER and NR band separation, while a low drift field may lead to pile-up and accidental coincidence (AC) events.

- Drift Velocity: Lower drift velocity affects time separation of scintillation and ionisation signals (respectively S1 and S2), influencing detection rates.

- Electron Cloud Diffusion: Lower drift velocity causes diffused electron clouds, impacting depth and planar reconstruction resolution.

3.3 The Xenoscope Facility

To demonstrate the viability of electron drift over a distance of 2.6 meters for the DARWIN project, Xenoscope, a dedicated demonstrator, was built at the University of Zurich. The demonstration of this drift distance is crucial for efficiently detecting and measuring the interactions of dark matter particles in the large volume of xenon. The main requirements consist in obtaining highly pure xenon for the setup in order to minimise background signals. Establishing a consistent vertical drift field ensures that electrons can efficiently reach the gas phase for signal detection. To this end, an efficient xenon purification system and a HV distribution scheme are meticulously tested [38]. Additionally, the installation of a top array of SiPMs enables the evaluation of their performance under cryogenic conditions and allows to test their potential use in the DARWIN project.

Other than its main objective of testing the electron drift, Xenoscope is ready for extended applications aiming to test diverse detector components for DARWIN. The focus is on two critical aspects: maintaining LXe purity and achieving a robust and uniform electric drift field. Improving the purity in the detector revolves around minimising electronegative impurities in the LXe, accomplished through continuous recirculation. We aim for an electron lifetime exceeding 1.75 ms [39]. Achieving a uniform drift field ($\sim$ 100V/cm) is pivotal for maximising electron migration to the gas phase, enabling the use of a liquid recirculation system.

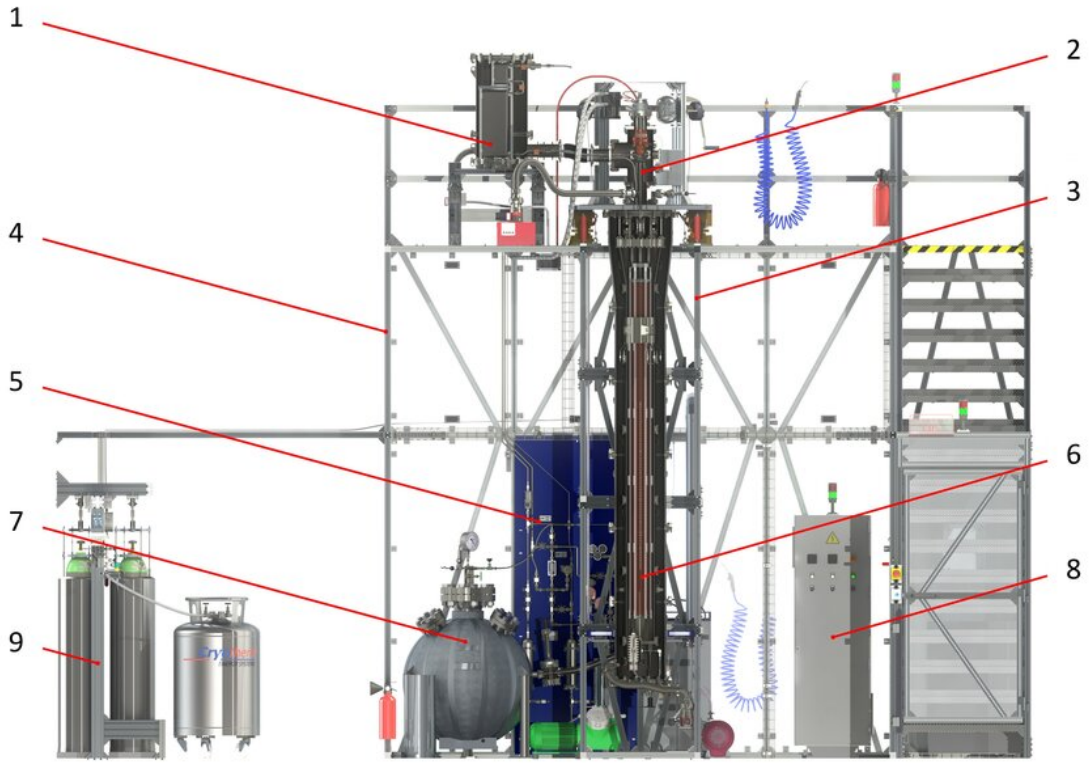

Figure 9: Rendering of the Xenoscope facility with all the main components. (1): Heat exchanger, (2): Cooling tower, (3): Inner frame, (4): Outer frame, (5): Purification gas panel, (6): TPC in the 24.8 cm diameter and 312 cm height cryostat, (7): Liquid recovery system, (8): Power distribution cabinet, (9): Gas recovery and storage system [4].

Allowing for systematic testing and optimisation of various components, the design and characterisation of Xenoscope is done over two steps, of increasing drift lengths: first a 50 cm purity monitor [40], then the current configuration of a 2.6 m TPC [25]. Realising such a high drift field in a 2.6 m TPC necessitates delivering HV ($\sim$ 50kV) to the cathode while considering safety, stability, and LXe temperature compatibility. Xenoscope serves as a testing ground for various HV systems to identify the optimal setup for DARWIN. Beyond electron drift demonstration, Xenoscope also facilitates benchmarking and parameter assessment crucial for DARWIN, such as longitudinal and transverse diffusion measurements, along with optical parameter investigations [4]. Additionally, Xenoscope offers a platform for collaborative activities within the DARWIN initiative, encompassing novel photosensor concepts and subsystem testing for the future DARWIN experiment.

4 The Silicon Photomultiplier Array

As a full-scale demonstrator, Xenoscope investigates many of the technological challenges raised in the DARWIN project. A key focus is the search for ultra-low background photosensors capable of detecting prompt scintillation light and charge signals in xenon. While current rare-event experiments employ PMTs for this purpose, Xenoscope allows to explore the use of SiPMs, advanced solid-state photodetectors that have gained significant attention in the DARWIN project research. This section presents a theoretical background on the working principle of silicon photomultipliers, as well as the results of a sensor testing campaign. This preliminary investigation serves as groundwork for a simulation focusing on the transport of electrons within the TPC and their detection using the SiPM array.

4.1 Working Principle of Silicon Photomultipliers

4.1.1 Semiconductors

There are multiple key parameters that are essential for understanding the operation of SiPMs. Since they are semiconductor devices, the starting point will be to give a short introduction into this concept.

A semiconductor is a material which can behave as a current conductor or insulator, making it ideal for a wide range of purposes. The diverse applications encompass light detection in astronomy, medical applications, and utilisation in high-resolution microscopy [25]. The arrangement and structure of atoms within a crystal's lattice are the key to understanding semiconductor behaviour. Typically, elements like silicon (Si), germanium (Ge), or compound semiconductors like gallium arsenide (GaAs) make up semiconductors. These substances are characterised by a regular arrangement of atoms that form a crystal lattice [41].

The band theory offers an essential framework for understanding the electronic characteristics of semiconductors. In free atoms, electrons are bound to the nucleus and exist in distinct energy states. The following process is represented in Figure 10. When atoms form a crystal, the discrete states of these electrons are grouped into two distinct bands: the valence band and the conduction band. The valence band is occupied by electrons at their lowest energy states at absolute zero temperature. Electrons with such energy levels are tightly bound to their parent atoms and contribute to the stable chemical properties of the material. Above the valence band lies the conduction band which represent higher energy levels that electrons can access.

Unlike electrons in the valence band, the energy levels accessible in the conduction bands allow electrons to move freely in the material, contributing to its electrical conductivity [42]. Between these two bands, there is a spacing defined as the energy band gap or the "forbidden gap" where electrons are absent, therefore creating a potential barrier. This gap is the defining characteristic for insulators and conductors. In conductors, the valence and conduction bands overlap, allowing electrons to move freely and conduct electricity in the material. This overlap results in high electrical conductivity as electrons can easily transition between the two regions.

On the other hand, insulators are defined by a wider energy gap, restricting the flow of electric current through the material, rendering insulators poor conductors. This difference of potential is specifically defined as an energy $E_G = E_V - E_C$, where E_V is the highest valence band energy and E_C is the lowest conduction band energy. In particular, an electron would need to acquire energy in the order of E_G to overcome the potential barrier and get transported to the conduction region.

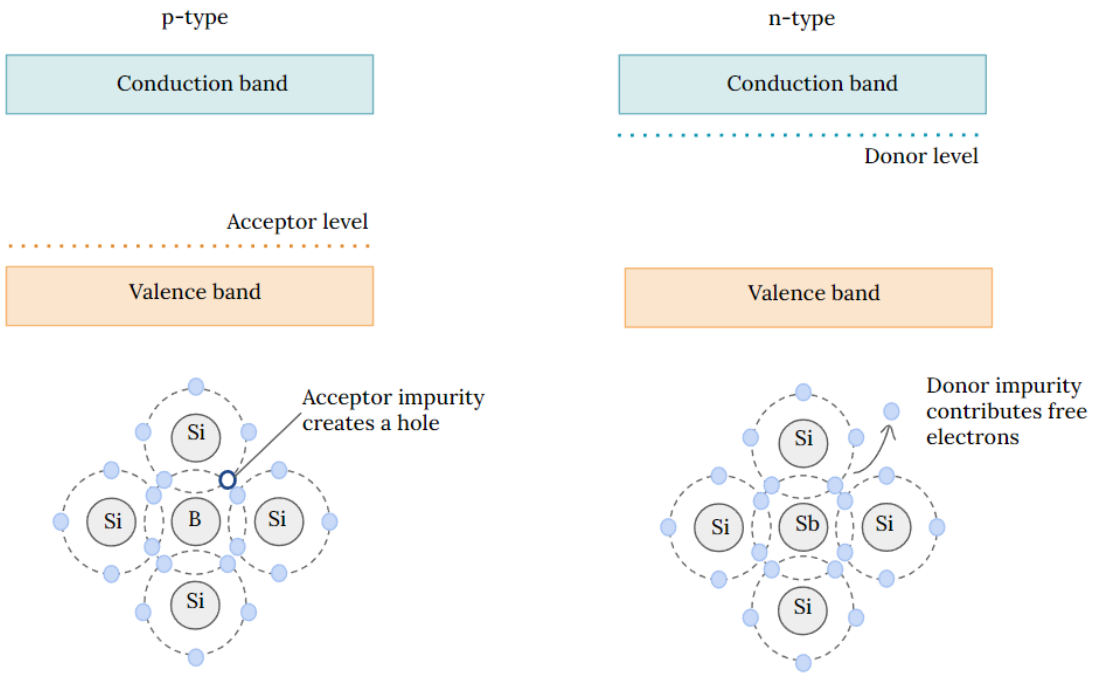

Figure 10: On the left: silicon lattice with a boron acceptor impurity, which leaves free-moving holes in the crystalline silicon structure. The acceptor atom creates a new energy state - the acceptor level - right above the valence band, which can be occupied by valence electrons through thermal excitation. On the right: silicon lattice with a donor impurity, which creates free-moving electrons in the silicon crystalline structure. The newly created energy level - the donor level - is below the conduction band. Figure adapted from [43].

Semiconductors represent an intermediate state between insulators and conductors in terms of their gap energy magnitude. Semiconductors display distinctive electrical characteristics because of this intermediate energy gap. At room temperature, thermal energy enables some electrons to cross the band gap and move from the valence band to the conduction band, increasing the conductivity of the material.

Through manipulation techniques such as doping, the electrical behaviour of semiconductor materials can be finely tuned to suit specific applications. The way to dope a material is to act on the concentration of free charge carriers, by intentionally introducing impurities or "dopants". Dopants used in semiconductors are of 2 types: electron donors (n-type), and electron acceptors (p-type). Among the most used n-type dopants are phosphorus (P), arsenic (As), and antimony (Sb), which introduce extra electrons into the semiconducting material. Common p-type dopants include boron (B), gallium (Ga), and indium (In), which create electron holes in the crystal lattice. The dopant concentration is also an important factor for semiconductor doping. The concentration of dopants is typically expressed in terms of the number of dopant atoms per unit volume. When the dopants are introduced into a material, dopant states are created within the band gap with new accessible energy levels. The conductivity of the material is, therefore, directly affected. These new energy states are called either acceptor level or donor level, as represented in Figure 10. A thermally excited electron can access the acceptor state right above the valence band. On the other hand, donor states located close to the conduction band act as energy levels that electrons from the donor atoms can transition into, becoming mobile charge carriers. Doping significantly changes the concentration of charge carriers that increase in n-type doping and decreased in p-type doping.

4.1.2 PN Junction

In a crystal, a PN junction refers to the interface created between a p-type semiconductor and an n-type semiconductor. When the two regions are assembled, the concentration gradient of the charge carriers causes a diffusion process. During diffusion, electrons from the n-type region are transported across the junction into the p-type region, while holes in the p-type region diffuse in the opposite direction and into the n-type region. This diffusion will go on until an equilibrium is reached. As electrons move to the P-region, they recombine with the holes, and vice versa. This recombination process leads to the creation of a depletion layer.

The depletion layer is a narrow area in the PN junction where the concentration of mobile charge carriers is significantly reduced. Because of the ionisation of impurities, there are immobile positive ions in the N-region and immobile negative ions in the P-side. These fixed ions create an electric field that opposes the further movement of charge carriers across the junction. Consequently, a potential barrier is established across the PN junction.

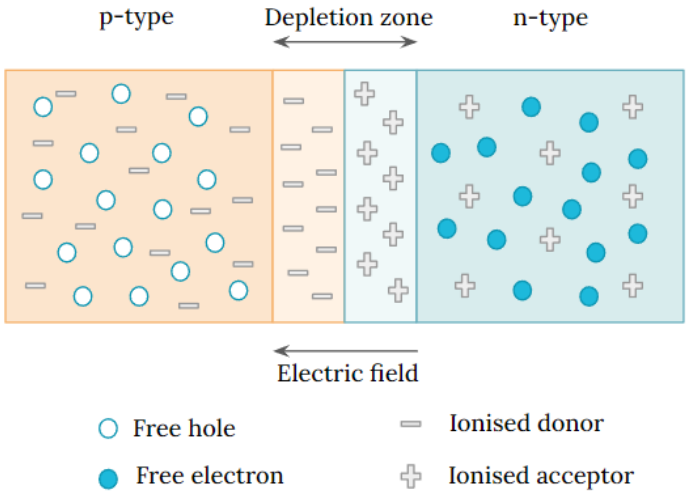

Figure 11: Diagram of P-N junction. Figure adapted from [43].

The magnitude of this potential barrier depends on the doping levels of the P and N regions. The Fermi energy levels of the P and N regions align in equilibrium, and there is no net diffusion of charge carriers.

Applying an external voltage to the PN junction changes its behaviour. When a forward bias is applied to the P-region and a reverse bias is applied to the N-side, the potential barrier is reduced, allowing current to flow across the junction. This forward biasing facilitates the conduction of electricity through diodes or transistors. Conversely, when a reverse bias is applied to the P-region and a forward bias is applied to the N-region, the potential barrier increases, hindering the flow of current across the junction. This reverse biasing makes the diode or transistor act as an insulator, preventing the flow of electricity.

4.1.3 Single APD and Geiger Mode

An Avalanche Photodiode (APD) is a diode using the same principle as a PN junction, but optimised for photon detection by amplifying weak optical signals. The avalanche photodiode effect exploits the properties of the PN junction in reverse bias mode.

In a PN junction, the depletion region widens when a reverse bias voltage is applied, producing a potent electric field across the junction. This electric field in a standard PN junction diode prevents the flow of current [44]. In contrast, a high reverse bias voltage is applied to the PN junction in avalanche photodiodes, producing a strong electric field. An electron-hole pair is produced when a photon with enough energy enters the depletion region and is absorbed by the semiconductor material there.

These charge carriers are accelerated by the electric field present in the depletion region. As the accelerated charge carriers gain energy, they acquire a sufficiently strong kinetic energy to extract additional electrons from the crystal through impact ionisation. The newly freed electrons are then accelerated by the electric field, thus creating even more electron-hole pairs. This process of impact ionisation followed by charge carrier multiplication is known as the avalanche effect. This effect is used to significantly amplify the original signal. A low photon count can generate a higher number of electron-hole pairs, resulting in a much higher current. This makes avalanche photodiodes highly sensitive to low-light conditions and allows them to efficiently detect weak optical signals.

4.1.4 Photon Detection by SiPMs

A silicon photomultiplier operates based on the principle of avalanche multiplication in a semiconductor material. SiPMs are composed of an array of APDs, referred to as a single MPPC pixel, each having its own quenching resistor, as illustrated in Figure 12. When a photon hits the silicon material, it creates an electron-hole pair within a cell. The electric field across the diode accelerates these charge carriers, leading to an avalanche of $10^5 - 10^6$ electrons. This multiplication process results in a rapid, self-sustained discharge that produces a significantly amplified current pulse, enabling the detection of single photons. The amplified avalanche signal within the SiPM pixel requires suitable amplification and readout mechanisms to convert it into a measurable output. This process involves monitoring the avalanche discharge to prevent the continuous flow of current. As represented in Figure 12, each pixel includes a quenching resistor R_Q , which rapidly reduces the voltage across the pixel, ending the avalanche process which allows the pixel to reset quickly for the next detection event.

SiPMs are characterised by several key performance characteristics in their application within detectors. Photon detection efficiency (PDE) quantifies the ability of the sensor to convert incident photons into detectable electrical signals. It is expressed as the percentage of incident photons that result in a registered response by the detector. Dark count rate (DCR) represents the frequency of avalanche discharges occurring in the absence of incident photons, influencing the overall noise level of the SiPM [45].

The probability of cross-talk, another key parameter, delineates the likelihood of simultaneous or near-simultaneous avalanches occurring in adjacent pixels. Gain, signifying the multiplication factor of the charge carriers within the avalanche process, serves as a crucial performance determinant. The breakdown voltage (BV) is a critical parameter characterising the SiPM. It corresponds to the specific voltage at which the SiPM transitions into the Geiger mode, initiating the avalanche multiplication process.

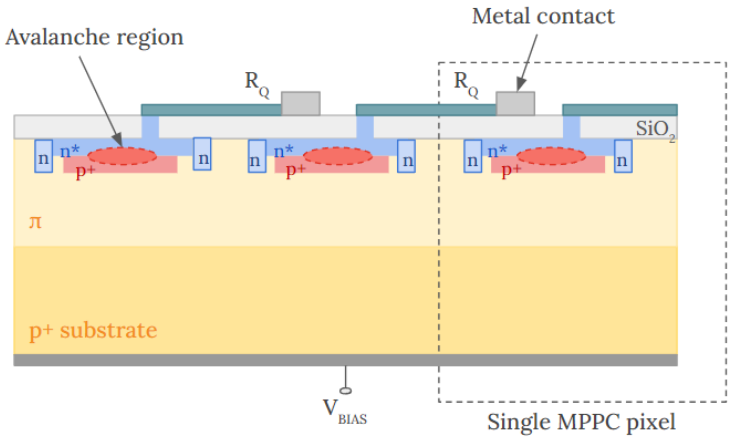

Figure 12: Working principle of a SiPM. An array of parallel-connected, identically sized microcells makes up a SiPM. A single APD is combined with a quenching resistor, RQ, to form a single microcell. Figure adapted from [46].

This value represents a threshold beyond which the energy received by an incident photon triggers a chain reaction of electron-hole pair creation and multiplication within a SiPM cell. When the applied voltage exceeds the BV, the avalanche effect results in an amplified electrical pulse that constitutes the output signal of the SiPM.

4.2 Integration of the SiPM Array

Xenoscope allows to investigate the use of a SiPM array as its only light sensor device for the S2 signal detection. These devices were first implemented in the Xurich II test facility [35], also a dual-phase xenon TPC. To qualify for integration into the DARWIN project, photosensors must satisfy a range of criteria. In the context of dark matter detection, the capability to detect low-energy recoils from WIMPs in xenon holds significant weight. These interactions yield relatively subdued light output due to their low energies (O(1 keV)) [25], hence the need for photosensors with the ability to detect individual photons. This requires high gain, a substantial photon detection efficiency (PDE), and precise single photoelectron (SPE) resolution. SiPMs also have a good VUV light detection efficiency similar to that of PMTs used until now. One of their main advantages is also their small size which is more efficient for position reconstruction.

The chosen model for the operation of Xenoscope is the VUV4 family of sensors [47] which is the most recent and the most improved model regarding PDE (from 10% to 24% at 175 nm) and cross-talk probability. Figure 13 shows the configuration of the array in 12 tiles. Each tile is composed of 4 quads, which makes a total of 48 quads in the array.

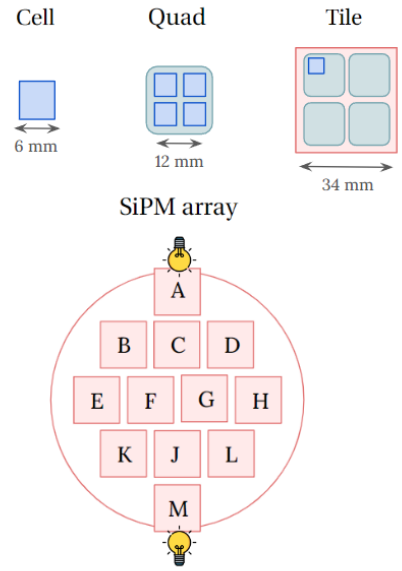

Figure 13: SiPM array configuration in Xenoscope: 12 tiles named A to M, 48 quad modules, and 192 6x6 mm² MPPC cells. The array is illuminated by light from LED transmitted through optical fibers positioned as shown in the Diagram.

A quad itself contains 4 6×6 mm^2 MPPC units from Hamamatsu (S13371-6050CQ-02 MPPCs) with a total sensitive area of 12×12 mm^2, so a total of 192 unit cells. Each cell is an independent operating unit, which role is to start and avalanche when a photon is absorbed. The four quads are fixed to printed circuit boards to form the tiles, collectively covering 36% of the total area with active sensors. These tiles are attached to a stainless steel plate to ensure their stability. The array is placed at the top of the TPC facing downwards, as it constitutes the top photosensor array which role is to detect the signal. The distance between the anode and the SiPM plane is set at 14.65 mm [47].

In this setup, all the sensors in a given tile area work together as a single unit, creating a larger active area. Combining multiple photosensor units into a single output expands the range of details that can be captured. This impacts the accuracy event position reconstruction, as illustrated in the simulation within Chapter 6. By consolidating signal amplification on-site, it becomes possible to decrease the necessary operational amplifiers. This presents an advantage, considering their power consumption and heat generation. Fewer amplifiers also mean fewer electronic parts, which helps keep radiation levels lower [24].

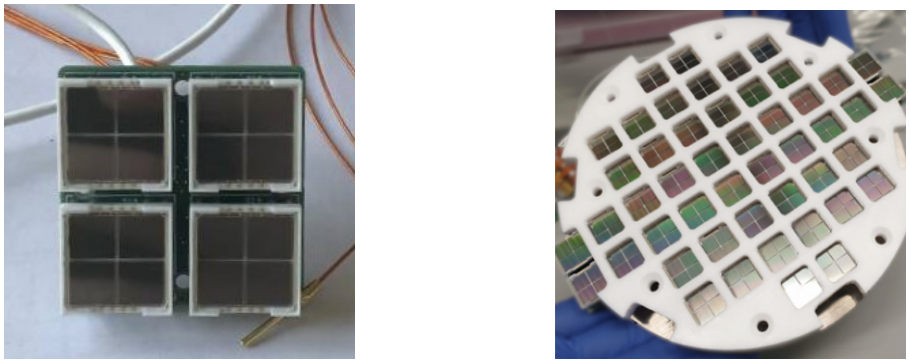

a) **b)**

Figure 16: a) Tile with mounted SiPMs. **b)** Fully loaded SiPM array. The tiles also serve as a structure holding the SiPMs, voltage distributors and pre-amplifiers for the signals. Images from [47].

4.3 Characterisation of the SiPM Array

The primary motivation behind the characterisation campaign is to collect SiPM data using the Data Acquisition (DAQ) system. To process the SiPM data, the PyLArS framework [34] was developed. This Python-based tool efficiently handles pulses originating from the detector's SiPM array data. It reads and interprets the output signals, providing a range of analysis tools for assessing key characteristics of the SiPMs, such as gain, DCR and CTP [25]. Currently, the framework is employed for consistency checks to ensure data integrity. In the future, it will be further utilised in the analysis of data collected during upcoming runs. This framework plays a critical role in data preprocessing, quality assurance, and the eventual extraction of valuable insights from the SiPM array data.

Among all the SiPM characteristics, the accurate determination of BV is crucial, as voltages above the BV are necessary for achieving efficient photon detection and maximising the gain of the SiPMs. The BV of a SiPM can vary among individual cells due to factors such as manufacturing processes, material properties, and operating conditions. As a result, meticulous calibration and adjustment procedures become necessary to establish consistent behaviour across the entire SiPM array. In the following section, we delve into the practical integration of an SiPM array within the detector. Subsequently, we detail the testing conducted on our SiPM array under vacuum conditions, within the detector environment. These tests are aimed at verifying the BV values and cross-validate them against findings from prior campaigns. In order to characterise the array, the bias voltage of the tiles is varied while maintaining a constant LED intensity, with the LED coming from the fibres as described in the Diagram 13. The objective being to determine the breakdown voltage values for all 12 tiles. The chosen settings for this test are collected in Table 1.

LED Configuration	
Amplitude	10Vpp
Frequency	500 Hz
Pulse Width	200 ns
Preamp Voltage	5V
Array Voltage	
Voltage Range	53 V to 57 V

Table 1: Settings for SiPMs measurements of BV characterisation.

The experiment is conducted under standard room temperature conditions, with the array installed within the TPC. Both the inner and outer cryostat components remain intact throughout the testing procedure. An example of the obtained waveforms in tile B is shown in Figure 17 for a signal triggered by LED pulses. Using this data, the maximal ADC count can be extracted for each intensity of the bias voltage to compute the BV associated to each tile.

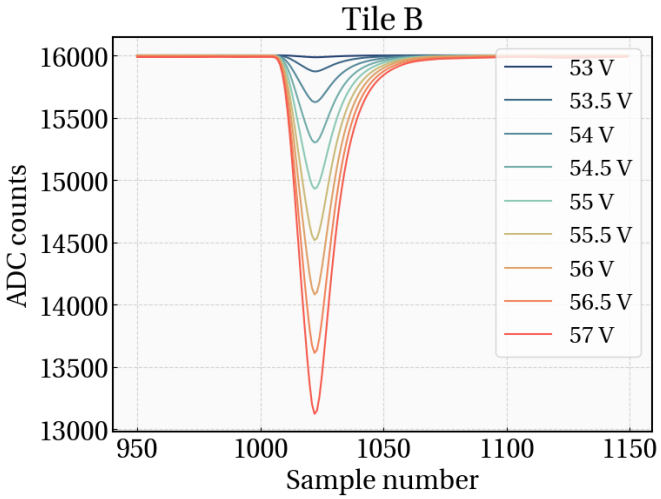

Figure 17: Examples of waveforms collected for different values of bias voltage.

In Figure 19, we compute the breakdown voltages of each tile for the chosen parameters through a linear regression. The values used for the fit range from 54 V to 57 V, excluding values below this range as the tiles are not yet operating in Geiger mode. Values above this range were disregarded due to saturation, resulting in a flattened curve and ultimately a biased outcome. The error bars on the plot are derived from the square root of ADC counts. The uncertainty values quantify the potential range of bias voltage where the ADC count transitions to the noise level.

Collectively, the measurements conducted, as detailed in previous characterisation campaigns [24, 25], confirm the successful installation and proper functionality of all twelve channels within the top array of Xenoscope. Furthermore, the computed breakdown values, as seen in Table 2 and Figure 18, align with the specifications provided by the manufacturer of $53\text{V} \pm 5$ [48].

Channel/Tile	**Breakdown voltage [V]**
01A	53.36 ± 0.02
02B	53.53 ± 0.04
03C	53.49 ± 0.04
04D	53.51 ± 0.04
05E	53.52 ± 0.04
06F	53.43 ± 0.03
07G	52.26 ± 0.03
08H	53.42 ± 0.03
09J	53.45 ± 0.04
10K	53.53 ± 0.04
11L	53.52 ± 0.04
13M	53.38 ± 0.09

Table 2: Computed values of BV for each Channel/Tile with deviations.

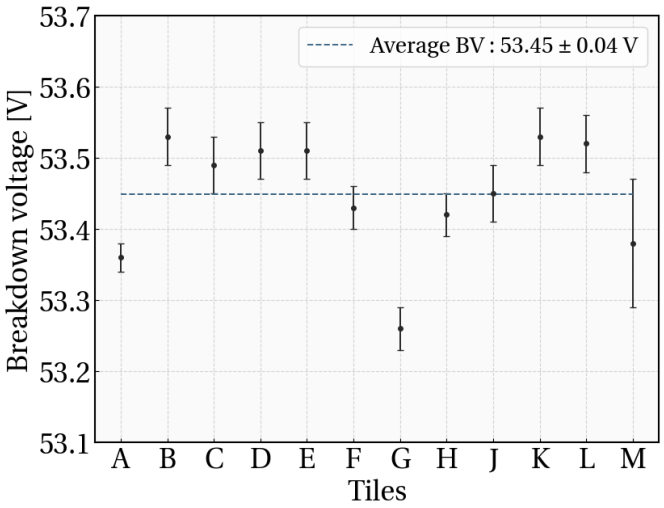

Figure 18: Collection of the breakdown voltage values for each tile while the array is installed in Xenoscope. The average value for the 12 tiles amounts to 53.45 ± 0.04 V.

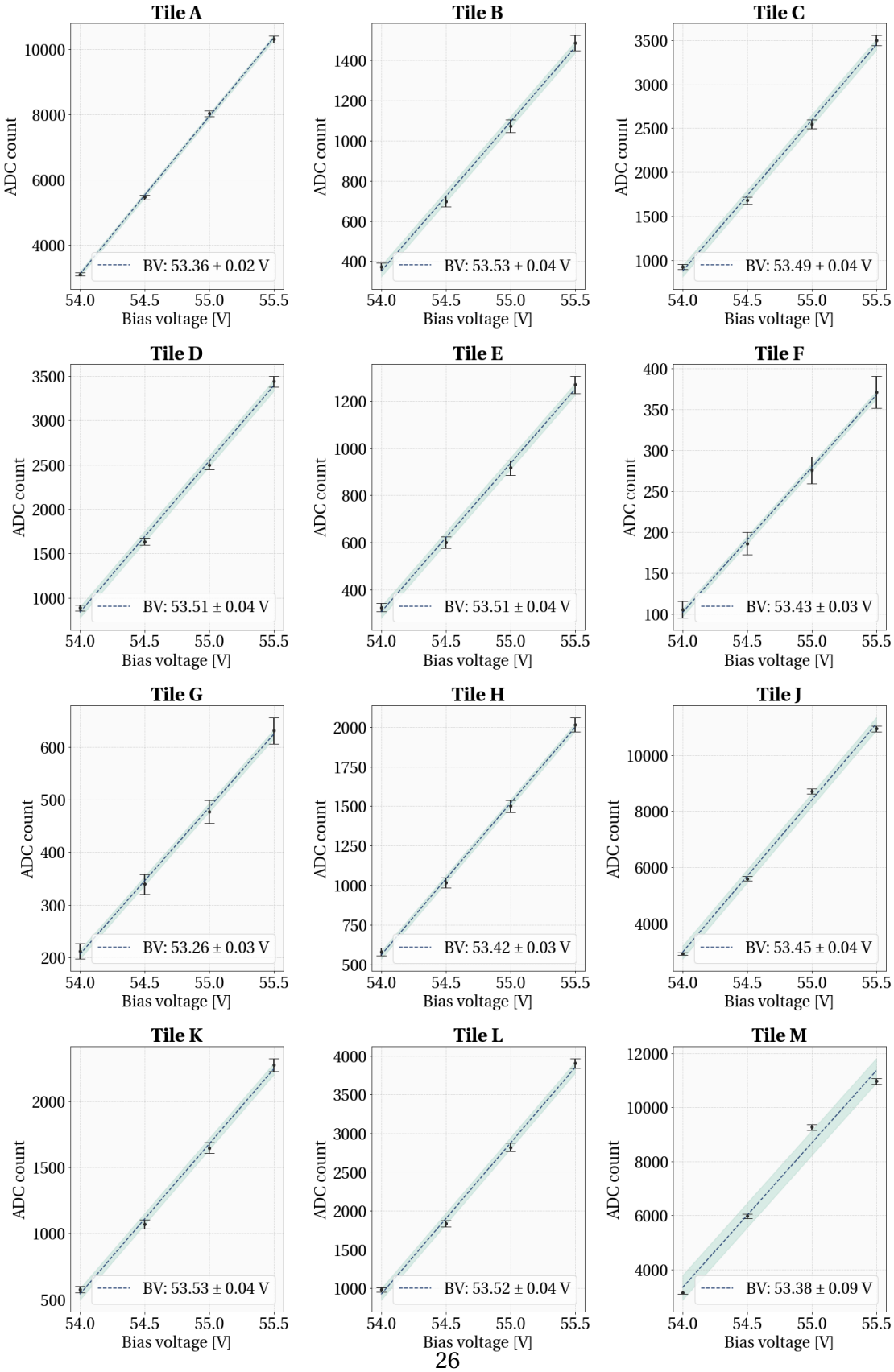

Figure 19: A linear regression between the bias voltage values and the peak amplitudes is performed to compute the breakdown voltage.

5 Signal Simulation and Detection

The upcoming goals of Xenoscope include quantifying the longitudinal and transverse diffusion of electrons emitted from the photocathode. The way to do do so is to study the drift and diffusion of electrons ejected from a photocathode illuminated by a pulsed xenon flash lamp [24]. Current efforts involve studying electron transport in the TPC when originating from other sources, such as internal or external radioactive for calibration purposes. In this section, the focus is to implement simplified simulation to gain insight into the interaction between gamma particles ejected from idealised gamma sources and xenon atoms in the liquid phase of the TPC. Further down the line of the analysis, the positions of these interactions are reconstructed and the accuracy of the reconstruction is evaluated depending on various parameters such as energy of the sources and their spatial distributions. This analysis is based on specific parameters associated with available calibration sources. So this serves as a fundamental step towards upcoming calibration campaigns.

5.1 Simulation Framework

Within this section, we present the relevant outcomes of an analysis using ideal sources as inputs, with a primary focus on examining the transportation of electrons generated through gamma interactions in LXe. In order to simulate the electron transport and predict the expected signals received by the top array, a framework called XenoDiffusionScope was developed [49] and is used in this study. The Diagram 20 recaps all the steps used in the simulation, and more details are given in the following sections. These steps are based on the working principle of a dual-phase TPC (Figure 7).

To begin, this investigation involves the selection of specific gamma energy peaks, in alignment with forthcoming calibration sources. The decision to focus on specific gamma energy peaks, rather than conducting an analysis of the entire spectra, is rooted in the context of this idealised study. While a comprehensive spectrum analysis holds inherent value, our central objective is to establish a fundamental comprehension of electron transport mechanisms within the TPC. By concentrating on distinct energy peaks, the investigation is narrowed down to specific interactions that are particularly illustrative of the underlying principles at play. This targeted approach grants a first insight into these mechanisms, before approaching realistic sources simulation. The idealised nature of this study allows to isolate and systematically examine the main steps of the simulation without potential errors stemming from full spectra analysis.

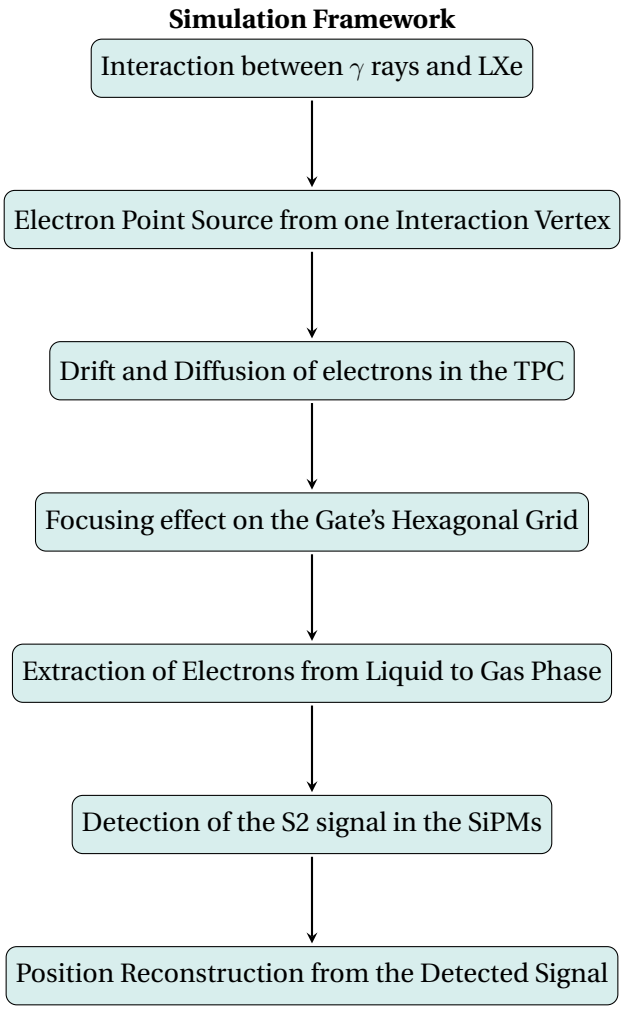

Figure 20: Flowchart of the XenoDiffusionScope simulation framework.

As seen in the Figure 20, electrons produced in gamma-Xe interactions are drifted through the TPC, taking into account longitudinal and transverse diffusion. When the electrons reach the gate, they are extracted from the liquid to the gas phase under the effect of the extraction field resulting in the production of a proportional S2 signal. Subsequently, the distribution of photoelectrons across the array can be obtained. This requires accounting for the gain from electrons to photoelectrons and the light collection efficiency map derived from each extracted electron position [24]. Summing the light patterns produced by the photoelectrons and integrating the resulting pattern across the sensitive area of SiPM photosensors generates the final pattern. This pattern holds the key to determining the $x - y$ position and spread of the initial electron cloud.

5.2 Drift and Diffusion of Electrons

5.2.1 Simulation of the Initial Electron Point Source

The study relies on the use of available gamma sources for forthcoming calibration campaigns of Xenoscope [50]. These gamma sources, namely ^{137}Cs, ^{133}Ba, and ^{57}Co, are selected for the analysis due to their well-understood decay properties and distinct decay peaks. As mentioned, the approach is to ensure robust and accurate calibration without introducing unwanted interference. Therefore, the simulation makes use of the specific gamma peaks of each source associated to the energy levels depicted in the Table 3.

In γ-decays, a nucleus initially existing in an excited state undergoes a transition to its fundamental state or another lower-energy state through the emission of a photon. Unlike α- or β-decays, this process does not alter the isotope itself, reflecting an analogy to the light emission during the deexcitation of excited atoms. While the energy level spacing in atoms is typically on the order of electronvolts, nuclear energy level differences are on the order of megaelectronvolts. Each isotope possesses a distinctive set of energy levels, yielding a discrete γ-ray energy spectrum that exhibits distinct and sharp peaks, akin to the spectral lines seen in atomic systems [51].

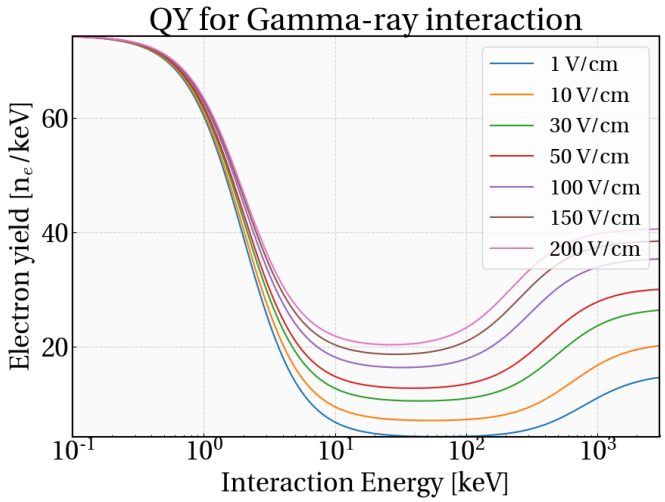

Figure 21: Charge yields (QY) obtained for gamma interactions using NEST framework v2.1.0 [52].

Isotope	E_γ **[keV]**	N_e
^{137}Cs	661.7	22618
^{57}Co	122	2482
^{133}Ba	81	1512

Table 3: Isotopes to be employed in future calibration campaigns of Xenoscope. The electron yield for each energy value is calculated given a value of electric drift field $E_{\text{Drift}} = 100$ V/cm. Energy values from [53].

The initial electron cloud is obtained using the the NEST (Noble Element Simulation Technique) framework, which accommodates the micro-physics of interactions within noble gas detectors [54]. The framework allows to simulate the outcome of gamma-induced ionisation within a xenon medium.

This is done by taking into account the properties of the detector, such as the chosen drift field. By inputting the gamma energies relevant to our calibration sources, along with the specific drift field used in the detector, the number of electrons in the initial point sources is retrieved and the values are presented in Table 3.

5.2.2 Diffusion Model and Transport Properties

Transport parameters	
Electric drift field	100 V/cm
Electric drift speed	1.364 mm/μs
Longitudinal diffusion coefficient	0.0027 mm^2/μs
Transversal diffusion coefficient	0.0057 mm^2/μs
Electron lifetime	200 ns
Extraction efficiency	99%

Table 4: The relevant parameters and constants used in the diffusion model as encoded in the XenoDiffusionScope framework [24].

The simulation framework employed in this study was built upon a selected set of transport parameters collected in Table 4, each playing an important role in characterizing the electron transport within the detector. The values used for longitudinal and transversal diffusion effects are based on the model from NEST v2.0.0 implemented in the first version of the XenoDiffusionScope framework. The electric field implemented in the simulation is chosen according to the intended value aimed for the operation of Xenoscope [4]. The electron lifetime is defined by the drift time after which the number of electrons is attenuated to 1/e and is set to 200 ns.

The sequence of events begins with incident gamma particles depositing energy in LXe, generating free electrons. These electrons then undergo a drifting process, traveling from the cathode to the gate. Additionally, the behaviour of the initial electrons is influences by both longitudinal and transversal diffusion. Longitudinal diffusion, occurring parallel to the electric field, contributes to the widening of signals as the drift distances increase [38]. On the other hand, the transverse diffusion takes place perpendicular to the electric field, impacts the detector's resolution in the $x-y$ plane. The diffusion effects are modeled in Equation 5.1 as random walks with standard deviation D_L and D_T for the longitudinal and transversal component, respectively [24]. As seen on the Table 4, the transversal diffusion coefficient is expected to be approximately twice as high as the longitudinal one. The variance of the gaussian distribution for each direction is given by $\sigma^2 = 2D_{T/L}t$.

$$n(\vec{x},t) = \frac{N}{4\pi D_T t\sqrt{4\pi D_L t}} \exp\left[\frac{-\left(x^2+y^2\right)}{4D_T t}\right] \times \exp\left[\frac{-\left(z-v_d t\right)^2}{4D_L t}\right]. \tag{5.1}$$

The simulation captures the diffusion process within discrete time intervals. The updates to coordinates x, y, and z are controlled by the diffusion constants presented in Table 4, while the overall behavior is determined by the diffusion Equation.

The inherent randomness enriches the variability of the outcome, leading to different outcomes across different runs. This effect will be specifically discussed within the context of position reconstruction, detailed in Chapter 6.

5.2.3 Extraction of Electrons

When the electrons reach the gate, they are extracted from the liquid to the gas phase. The extraction process considers two effects: extraction efficiency and charge-focusing by the electrode grids [24]. The extraction efficiency correction is calculated based on a user-defined extraction efficiency parameter. As seen in Table 4, this value is set to 99%. The charge-focusing effect is complex and depends on the geometry of the electrodes, particularly the gate and anode electrodes, which are regular hexagonal meshes in Xenoscope. From previous studies, it is anticipated that the electrons tend to converge towards the centres of the hexagons constituting the gate [55]. To incorporate this effect, a model is established by determining the positions of the hexagonal centres, based on user-defined parameters such as hexagon side length and grid radius. Electrons initially situated within a specific hexagon are then shifted to the centre of that hexagon, located at z_{gate}.

E_γ**[keV]**	**Initial yield**	**Extracted electrons**	**Photoelectrons**
81	1512	577	16,484
122	2482	947	27,055
661.7	22618	8,632	246,616

Table 5: Initial electron yield, number of extracted electrons and calculated number of photoelectrons using single electron gain.

To illustrate the impact of the charge-focusing effect, a selection of events corresponding to the energies of the considered isotopes in Table 3 is chosen. The final positions of the electrons are constrained to the 2787 centres of the hexagonal grid. Notably, the points after the diffusion process are subsequently shifted to the centre of the nearest hexagonal unit, highlighting the influence of the electrode grid geometry. Figure 22 demonstrates an event involving electrons released from a potential interaction between ^{57}Co and xenon atoms. Various z values are examined to highlight the impact of transversal diffusion, which is more pronounced than longitudinal diffusion. For a more detailed perspective on the points within the focusing plots, the corresponding visualisations can be found in Figure 36. In a TPC, charged particles drift along the electric field, causing lower longitudinal diffusion due to the predominant guiding effect of the electric field. Conversely, transversal diffusion, occurring perpendicular to the drift direction, is higher as the electric field has less influence on this motion.

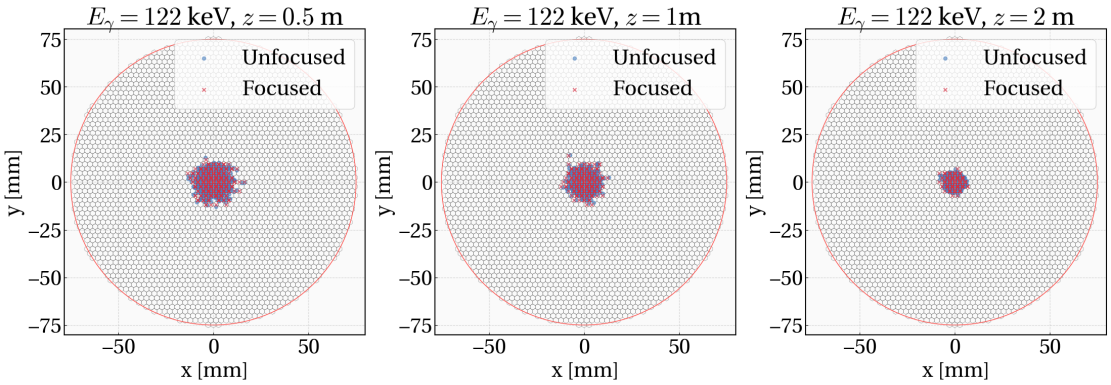

Figure 22: Illustration of charge-focusing effect in Xenoscope for a $E_\gamma = 122$ keV with initial positions $(0, 0, z)$ with $z = 0.5, 1, 2$ m to visualise the diffusion effect for different heights. The electron positions are depicted after undergoing drift and diffusion. The different colored points represent the effect of the focusing process. The diffusion process spreads out the events, while the focusing shifts the points to the centre of the closest hexagonal unit in grid. The outer red line corresponds to the TPC radius.

However, it is important to acknowledge a limitation associated with this approach. In instances where events are positioned near the edge of the TPC, the charge-focusing effect can lead to a counter intuitive outcome. Specifically, the electrons tend to converge back towards the gate electrode due to the focusing mechanism. Note that the data points, before and after focusing, represent clusters of multiple electrons as the overall number of extracted electrons have to correspond to the values written in Table 5.

5.3 Signal Detection on the Top Array

5.3.1 Simulation of Light Signals

As electrons transition from the liquid to the gas phase, they trigger a proportional scintillation effect, generating the S2 signal. This signal is captured in the photosensors, which record amplified ionisation response. The next step of our simulation is therefore to convert these extracted electrons situated at the gate, into proportional scintillation light. In this process, we make the assumption that the emission of scintillation photons is isotropic around the position of the extracted electron. In order to quantify this scintillation light, we need to account for the number of photoelectrons. Photoelectrons (PE) refer to electrons that are detected by the photosensors, taking into account considerations related to photon detection efficiency. Within the proportional range of the photosensor, the quantity of photoelectrons is directly proportional to the number of incident photons striking the photosensor.

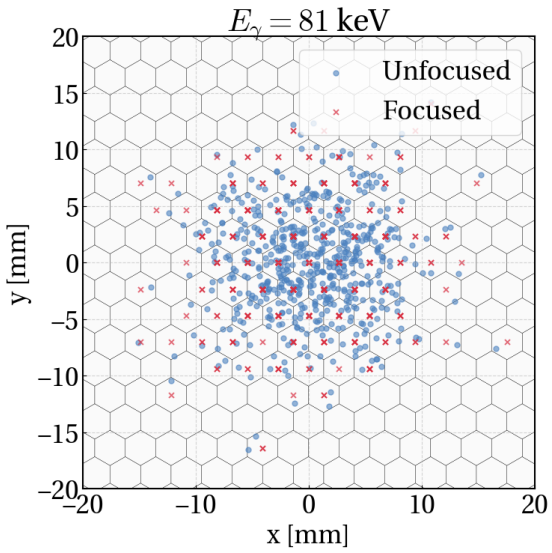

Figure 23: Extracted electrons from an $E_\gamma = 81$ keV event where positions are shown before and after the focusing effect.

Converting electrons to photoelectrons can then be used as a unit of measurement for detected photons in this context. This conversion is done using the empirical value derived from the Xurich II experiment, which characterises the gain for a single electron as 28.57 PE [39]. This value applies to Xenoscope as the extraction field is the same as in Xurich II, the SiPMs were also integrated as photosensors albeit in a different geometry.

Once the number of resulting photons is collected, the next step is to construct a light collection efficiency (LCE) map, meaning the spatial-dependent probability that a photon produced at a given position hits a photosensor. An example of one light collection efficiency map is presented in Figure 24 where a light signal resulting from one grid point is computed.

The key for computational efficiency is to take into account the fact that events will happen in the constrained number of hexagonal centres of the mesh grid. It is sufficient to compute the light pattern produced by one hexagonal unit, and scale it to the number of photoelectrons located at that specific point. Given that all electrons contribute uniformly to the signal, the intensity registered by a sensor is proportional to the quantity of electrons associated with each hexagonal point. Following this process, we can use the LCE maps to construct the light pattern resulting from our initial events as seen in Figure 25, where the signals are simulated for different z values. For a closer examination of the pre-sensor patterns, refer to the plots shown in Figure 37 in the Appendix section (Appendix 8.2).

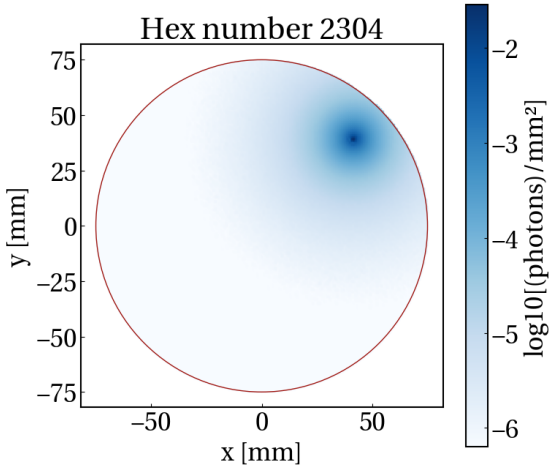

Figure 24: Example of a LCE map for hexagonal unit number 2304. As described in the text, toy events representing photon hits are simulated. The distribution is then normalised to the number of photons produced and the pattern is interpolated.

This collective signal is then applied to the chosen sensor configuration to accurately represent the scintillation response.

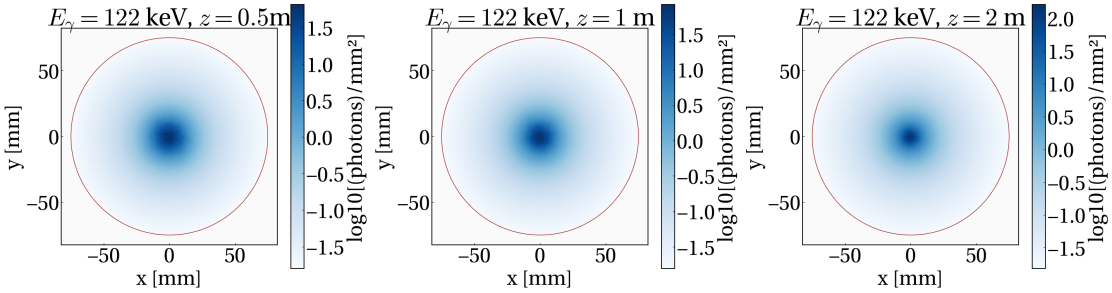

Figure 25: The interactions correspond to the scenarios illustrated in Figure 22 to show the diffusion effect at different heights.

5.3.2 Hit Patterns on the Photosensors

In practice, the configuration of the sensors allowing us to view the signal is not as small as the grid points chosen for the computation of the patterns in Figure 25. As discussed in Chapter 4, the photosensors are organised in an array of 12 tiles containing 12×12 mm^2 MPPC quad units. This model with 48 quads was reproduced in the simulation and the patterns are integrated in the sensitive area delimited by the photosensors. The Figure 26 presents the results obtained for the considered events. In order to optimise the measurement of transversal diffusion in future campaigns, this area of the analysis (granularity of the simulated photosensors) should be explored more into detail.

Our main objective is to reconstruct the interaction positions from selected events which is presented in the following section.

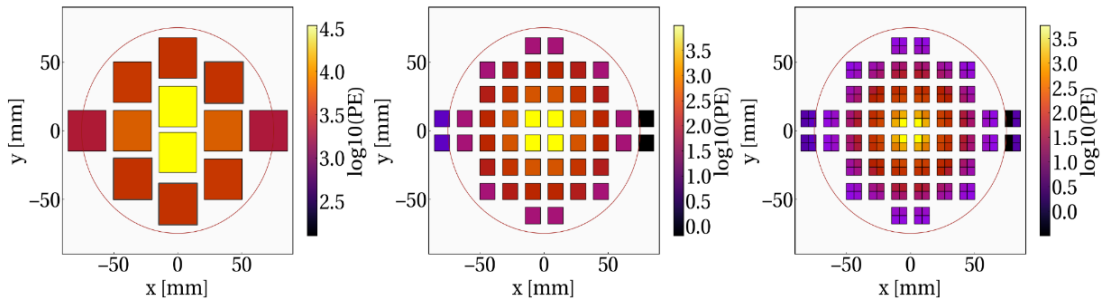

Figure 26: Patterns obtained from the an initial event with $E_\gamma = 122$ keV with initial positions of the electron source given by $(0, 0, 0)$. Different configurations of the array are shown.

The simulation operates under certain assumptions, which ultimately have an influence on the intermediate and final results. The implications arising from these assumptions will be addressed in Section 6. To summarise, one notable assumption relates to the uniformity of the electric field across the wall and electrodes of the detector. It is worth noting that the drift field, as explored in Xenon detectors, encounters distortion effects near the boundaries [56]. Several optical parameters such as reflections, scattering, and absorption, could also introduce complexities that are currently unaccounted for in the analysis.

6 Position Reconstruction

Building upon the established electron transport framework for Xenoscope, this section focuses on applying and evaluating an algorithm for reconstructing interaction positions within the detector.

The process of reconstructing the three-dimensional position within a TPC involves several critical factors. The z coordinate is an essential parameter that can be determined through the drift time of ionisation electrons. This is achieved by calculating the time difference between $S1$ and $S2$ signals, with the use of the field-dependent drift velocity in liquid xenon.
To initiate the process of reconstructing initial positions, we start by introducing the center of gravity algorithm. This algorithm stands as a simple yet effective tool for position reconstruction in dual-phase xenon detectors [57]. Subsequently, we put the algorithm into action by applying it across diverse scenarios that involve modifying initial conditions. These scenarios involve adjusting the initial mapping of transversal positions, variations in the interaction height, and modifying the interaction energy (associated with specific radioactive sources). The aim is to evaluate the effectiveness of the algorithm and its responsiveness to distinct factors affecting the reconstruction process in the Xenoscope setup.

6.1 Center of Gravity Algorithm

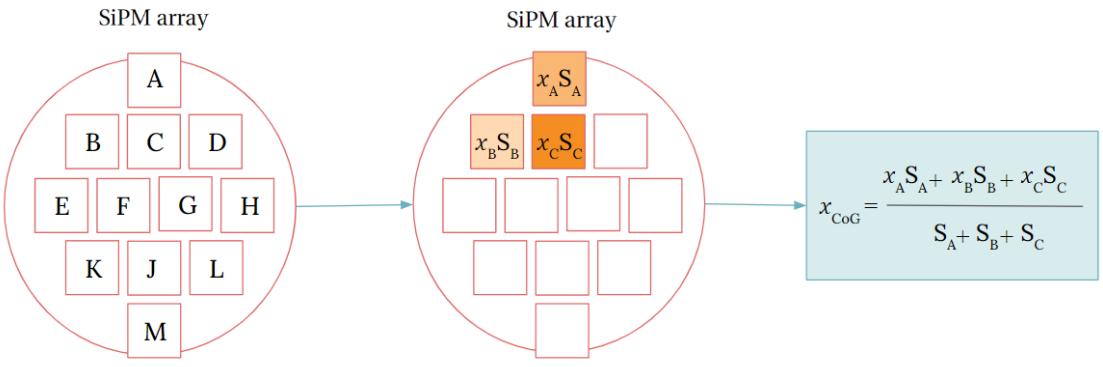

Figure 27: Diagram illustrating the position reconstruction algorithm based on the photosensors configuration in Xenoscope. In this example, the initial interaction is detected in the A, B and C photosensors.

The Center of Gravity (CoG) algorithm is a common method used for position reconstruction in the detector.

The algorithm is based on the principle of calculating the weighted average of the sensor positions to estimate the x and y coordinates of the initial event position. The CoG algorithm is constructed in a way to account for partial signals received on each sensor. In the context of SiPM arrays, the CoG method assigns to each term a weight S_i based on the partial signal by the sensor i. The CoG algorithm follows these steps:

1. Obtain the signals S_i from each sensor, where $i = 1, 2, \ldots, N$ and N is the total number of sensors in the detector.

2. Compute the weighted average of the x and y coordinates:

$$x_{\text{CoG}} = \frac{\sum_{i=1}^{N} S_i \cdot x_i}{\sum_{i=1}^{N} S_i}$$

$$y_{\text{CoG}} = \frac{\sum_{i=1}^{N} S_i \cdot y_i}{\sum_{i=1}^{N} S_i}$$

3. The reconstructed position of the initial event is given by $(x_{\text{CoG}}, y_{\text{CoG}})$.

The diagram in Figure 27 illustrates the steps of the CoG algorithm. First, the signals S_i from each sensor are obtained. Then, the algorithm proceeds to calculate the weighted average of the x coordinates (x_{CoG}) and the y coordinates (y_{CoG}). The estimated position of the initial event is output as $(x_{\text{CoG}}, y_{\text{CoG}})$.
For each reconstructed transversal position, the bias will be computed as the distance from the initial simulated positions and denoted Δr:

$$\Delta r = \sqrt{(x_{\text{CoG}} - x_{\text{initial}})^2 + (y_{\text{CoG}} - y_{\text{initial}})^2} \tag{6.1}$$

This value serves as the metric for the resolution comparison across the varied simulation assumptions discussed in the following sections.

6.2 Dependence on Initial Positions

6.2.1 Transversal Plane

An important aspect of the position reconstruction process lies in understanding its sensitivity to the transversal plane, defined by the chosen mapping of x and y coordinates. In this section, we compute the reconstruction bias by evaluating the dependency on the initial x and y positions. A mapping of the x and y coordinates is done, with 1060 distinct points.

At each of these points, 50 simulation runs are conducted. To capture the essence of the variability introduced by diffusion, the median is chosen as our representative value for Δr. This choice acknowledges that reconstructed positions can vary due to the stochastic nature of diffusion. The impact of computing the reconstruction bias for different initial positions is shown in Figure 28. This selection showcases only the scenario where $z = 2$m and the initial electron count is fixed. The height z is set with the reference point on the ground level, increasing as we ascend within the TPC, as seen in Figure 7. These plots show the outcome when the initial electron cloud contains $N_e = 2482$, which would be associated to the introduction of a cobalt source (as seen in Table 5). Among the different array, we are focusing on the quads and tiles setups. As the differences are not distinguishable solely based on the plots, the results for other energy scenarios and z values are collected in Appendix 8.3. Depending on the transverse initial positions, a significant observation emerges: the CoG algorithm shows a clear inward reconstruction bias. Notably, as positions approach the center, the value of Δr decreases, resulting in more accurate reconstructions. This phenomenon is also tied to sensor configuration, where the arrangement of tiles and quads distinctly influences the values of the reconstruction bias. It becomes clear that precision increases when interactions happen close to the center of a given sensor, reflecting the combined impact of the algorithm and sensor distribution. On the edges of the array, reconstruction accuracy drops by a factor of 5 compared to the central region, an outcome attributed to both algorithmic behavior and sensor design.

Additionally, our analysis highlights a pattern consistent with the array configuration. A stronger reconstruction is also demonstrated when initial interactions occur between sensors. This observation suggests that the signal distribution across multiple sensors enhances detection accuracy. However, it's important to critically evaluate our choice of using approximately a 1000 grid points and conducting 50 iterations per grid point. This decision prompts us to weigh the trade-off between grid point granularity and iteration count. While a finer grid may seem like the obvious choice to obtain more detailed insights, it also demands greater computational resources and does not guaranty a more accurate representation. In appendix 8.3, we display the results for the simulation ran with 10000 grid points and no iterations. Conversely, employing a coarser grid may accelerate computations but could compromise the precision of results by giving less coverage of the array.

6.2.2 Longitudinal Coordinate

The analysis of the impact of the initial interaction height on position reconstruction is portrayed in figure 29. This graphical representation illustrates the reconstruction bias as the initial interaction height varies within the TPC volume. The values of z are varied from 0 to 2 m, to encompass the possibilities for the placement of the radioactive source in future calibration campaigns.

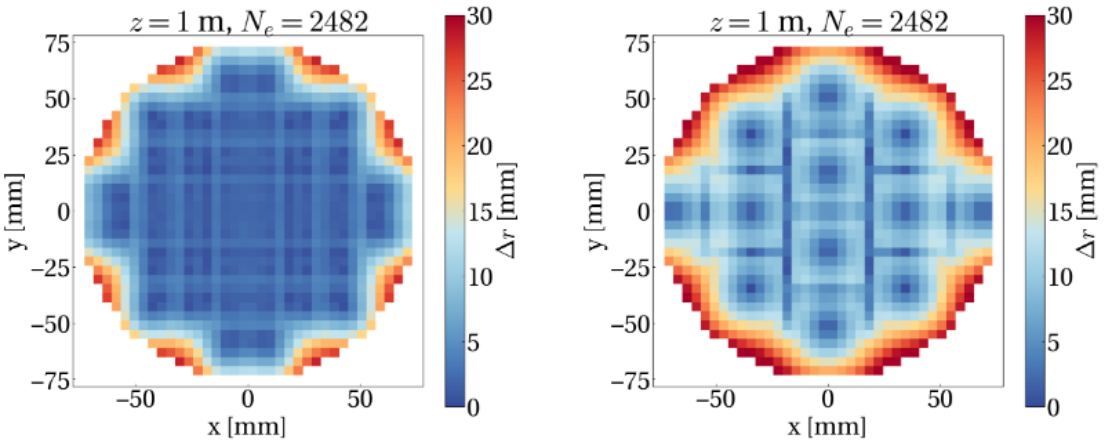

Figure 28: Position reconstruction bias maps: the plots depict the reconstruction bias, represented as Δr, over a grid of initial points (x, z) of the interaction vertices. The two maps are computed for $z = 1$m, representing the height of the interaction from the bottom of the TPC, and $N_e = 2482$, the number of electrons in each 122 keV point source.

The results are shown in separate curves for three distinct values of N_e representing the initial number of electrons in the vertex. These N_e values are chosen to align with gamma energy levels from the well-defined calibration sources, a topic detailed in section 5. The data points correspond to the median over 200 iterations for each entry of the initial position. The error bars represent the standard deviations associated with each distribution. To limit potential biases within the results, the initial transversal position is deliberately set at the central point of the TPC where $x = 0$ and $y = 0$. This choice does correspond to the optimal (or the least favorable) reconstruction position as it is not aligned with the center of a sensor. This decision also ensures that any impact from the lack of field uniformity effects is minimised, as it is unaccounted for in the framework at the moment. The reconstruction bias Δr is computed within the quads configuration on the top array.

The first observation from figure 29 is that the reconstruction bias demonstrates a decrease with higher z values when the interaction stems from the $E_\gamma = 81, 122$ keV energy peaks. More specifically, the variation around the standard deviations values decrease. This is due to the reduced drift and diffusion times experienced by the electrons during their transport within the detector volume.

When running the simulation for the drift described by Equation 5.1, the coordinates are updated at each time step, until the z coordinate reaches the height of the TPC. The time step is chosen to be $\Delta t = 0.1\mu$s. When the source is closer to the top of the TPC, which corresponds to higher z values, the electron cloud experiences less diffusion as represented in Figure 36.

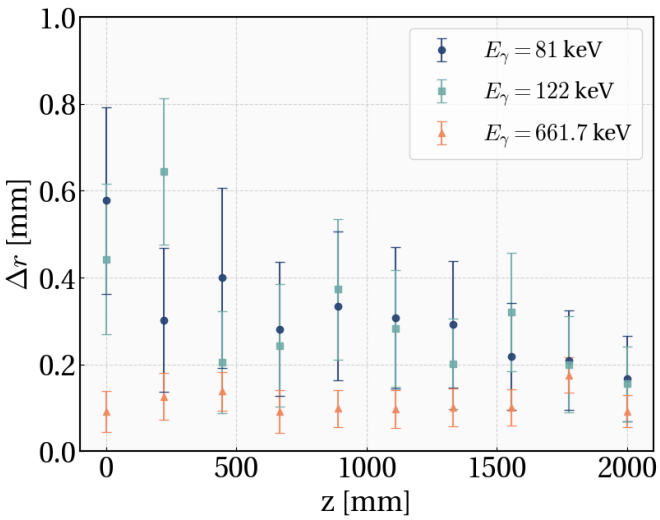

Figure 29: Position reconstruction bias (Δr) as a function of the initial interaction longitudinal position (z) for different initial electron counts. The initial positions of the interactions are given by $(0, 0, z)$ where z is varied from 0 to 2 m.

Notice that the reconstruction bias does not show a distinct decrease when the initial interaction comes from the $E_\gamma = 661.7$ keV peaks, i.e involving 22618 ionisation electrons. These increased statistics lessen the effect of the interaction heights. This aspect is discussed in the following section. The second characteristic acting on the reconstruction bias is the number of electrons involved in the initial event. The results manifest an expected correlation between the reconstruction bias and the number of electrons in the initial point source. Specifically, the algorithm exhibits enhanced precision and reliability with increasing electron numbers, corresponding in our case to more energetic sources. This phenomenon stems from the increased collection of photoelectrons, leading to more distinct and well-defined patterns on the photosensors. The computation therefore benefits from a larger and more reliable data set. The results linked to the point source variations are also explored in the following section.

As described in Chapter 5, the simulation inherently involves randomness. This randomness results in variations between different simulation runs, even when using the same initial conditions. Consequently, the computed values at each step of the simulation may slightly differ across runs due to the stochastic nature of diffusion. It is essential to point that the observed results, while indicative, are not characterised by the utmost precision. The center of gravity algorithm employed in the position reconstruction does possess inherent limitations which impact its accuracy. In order to refine reconstruction accuracy and specifically mitigate issues related to inward reconstruction, modifications to the fundamental expression of Equation 3 are necessary.

These modifications would involve adding flat-fielding coefficients to the expression. These coefficients compensate for disparities in gain and quantum efficiency across the photosensor array [57]. However, the most prominent source of uncertainties stems from the stochastic nature of the diffusion process, which is random by construction. In order to acknowledge the statistical nature of the electron transport process, the error bars are determined by calculating the standard deviation of the distribution for each initial position. As a representation of this characteristic, the 2D histograms for the construction bias as a function of the position is displayed in Figure 30.

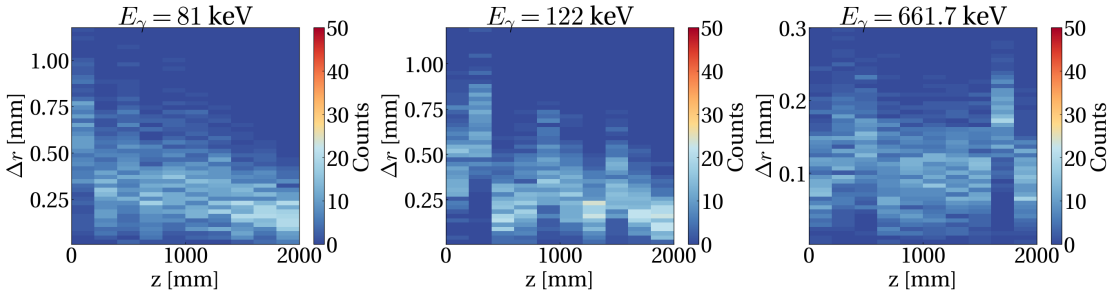

Figure 30: Position reconstruction bias (Δr) as a function of the initial interaction longitudinal position (z) for different initial electron yields.

In summary, the examination of the influence of initial interaction height on position reconstruction within the Xenoscope TPC provides quantifiable insights. A notable quantitative trend is the consistent decrease in reconstruction bias with higher source positions, especially evident in the transition from 0 m to 2 m. This quantifiable reduction in bias, from 0.6 mm to 0.2 mm, aligns with expectations of decreased electron drift and diffusion times at elevated heights. The data-driven correlation highlights the potential for optimising position reconstructions in future calibration campaigns and underscores the impact of source height on precision. Despite these considerations, further refinement of the analysis is required to account for the stochastic nature of the electron transport in a dual-phase Xenon TPC.

6.3 Dependence on Initial Interaction Energy

Following the methodology detailed in the previous section, the effect of the initial interaction energy on position reconstruction is explored. Specifically, the computation of Δr values has been performed for an array of electron yields involved in the initial interactions. These interactions span the range of electron yields from 0 to 24000, encompassing the values relevant for our chosen interaction energies. Similar to the z-dependency plot depicted in figure 29, the obtained data points correspond to the median Δr value computed over 500 iterations of consistent initial conditions. The error bars represent the standard deviations of this distribution.

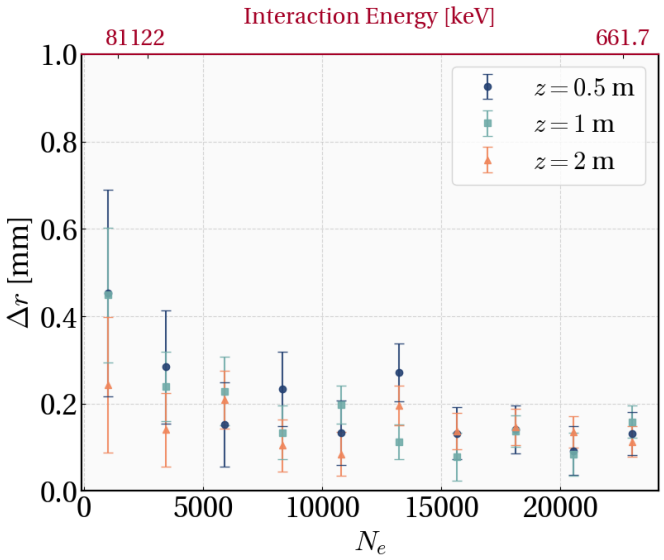

Figure 31: Position reconstruction bias (Δr) as a function of the number of electrons in the initial point source (N_e). The associated energy values of the calibration sources as described in section 5 are also displayed. The initial positions of the interactions are given by $(0, 0, z)$ where $z = 0.5, 1, 2$ m.

The main trend observed is a decrease in Δr magnitude with an increasing amount of electrons. More specifically, a prominent feature is the reduction in standard deviation values. All electrons share the same properties and undergo identical drift and diffusion processes. This, coupled with the 200 iterations of each entry, substantially enhances simulation statistics, leads to minimised fluctuations around the median. An additional observation shows the lack of impact from the z value on reconstruction bias as the values of N_e increase. With higher statistics, the influence of height variation is less important, and data points tend to converge towards the median.

Hence, within this constrained analysis, the variation of the energy source bears a more pronounced effect compared to fluctuations in the z position of the source. This correlation stems from the fact that choosing a high energy source increases the number of involved electrons, resulting in a more intense signal and subsequently, improved reconstruction accuracy. On the other hand, elevating the source acts on the diffusion effects, yielding a more compact signal albeit without an associated intensification of the signal.

This phenomenon is visible on the histograms illustrated in Figure 32, featuring results for the three distinct z values. To ensure a faithful comparison, the selected binning parameters are equal to the values used in the plots of Figure 30. A clear distinction emerges in the distribution spread between the z-dependent and N_e-dependent analyses.

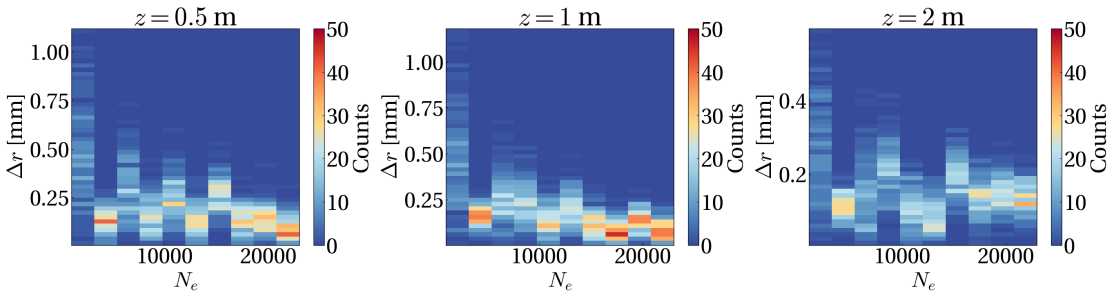

Figure 32: Position reconstruction bias (Δr) as a function of the number of electron yield (N_e) associated to the interaction energies between gamma particles and Xenon atoms.

Notably, even at lower N_e values, the Δr values exhibit greater concentration around the mean. As previously indicated, the variation in z is comparatively less effective, with plots displaying a median Δr of approximately 0.25 mm for $z = 0.5, 1$ m, and a median around 0.2 mm for $z = 2$ m.

In summary, the detailed exploration of the initial interaction energy's impact on position reconstruction has provided valuable insights. The observed trend of decreasing Δr magnitude with increasing electron yields indicates a pronounced correlation between source energy variation and improved reconstruction accuracy. This correlation surpasses the influence of fluctuations in the z position of the source, highlighting the significance of choosing a high-energy source in achieving more precise reconstructions. The histograms in Figure 32 vividly illustrate the concentrated distribution of Δr values around the mean for varying electron yields, emphasising the effectiveness of higher source energies in minimising reconstruction discrepancies. Overall, the analysis underscores the critical role of initial interaction energy in shaping the accuracy of position reconstructions, showcasing a notable reduction from 0.45 mm to 0.1 mm in Δr as the interaction electron count increases from 1000 to over 20000.

7 Conclusion and Outlooks

7.1 Work Highlights

The existence of dark matter is deduced from astrophysical and cosmological observations, revealing the presence of an invisible, non-luminous entity that influences the structure of the Universe. While the Standard Model prevails, the idea that dark matter consists of particles emerging from new physics gains attraction, with WIMPs among the leading candidates. In direct detection, large liquid noble gas targets, such as employed in dual-phase xenon TPCs, lead the way in sensitivity. While these detectors have set strong limits on WIMP interactions, the quest for direct detection is still ongoing. In this context, DARWIN emerges with a resolute mission. Equipped with a 40 t xenon dual-phase TPC, DARWIN sets its goal on unraveling the entirety of the accessible parameter space for dark matter. Among its R&D activities, a specific focus resides on the exploration of SiPMs as potential photosensors for the top array. These photosensors are responsible for detecting light resulting from the excitation and ionisation of the target medium. To assess the feasibility of this installation, this work was conducted in various steps to gain insights into the functioning of SiPMs in this role:

- **SiPM array testing and breakdown voltage determination:** The functionality of the SiPM array in Xenoscope was systematically tested, leading to the calculation of the breakdown voltage of the tiles in the array. The derived value, approximately 53 V, closely aligned with both prior measurements and the manufacturer's specifications.

- **Simulation of gamma ray interactions:** A simulation was conducted to replicate the outcomes of interactions between gamma rays and xenon within the detector. The simulation included the creation of electrons via ionisation, their subsequent drift, and eventual extraction into the gas phase. The resulting proportional scintillation generated a distinct S2 signal on the photosensor array, effectively captured and illustrated by the SiPMs.

- **Signal reconstruction using centre of gravity algorithm:** The signal captured by the SiPM array was subjected to a reconstruction process employing a CoG algorithm. The influence of initial positions and initial energy of gamma sources on the reconstruction accuracy was studied. The $x - y$ reconstruction revealed that the centers of the sensors were most effective for signal reconstruction, while inaccuracies were observed at the edges of the array. The resolution is estimated to be at 0.7 mm at the centre of the photosensors and culminating at more than 25 mm towards the edges.

This effect is both attributed to the inherit properties of the algorithm and the configuration of the photosensors.

- **Height and energy dependency of reconstruction:** An exploration of the source's height dependency unveiled significant insights. Analysing the initial interaction height revealed a distinct quantitative trend: there is an overall decrease of 66% in reconstruction bias when the source is positioned at ground level compared to being located 60 cm away from the photosensor array at the centre of the TPC. This aligns with reduced electron drift and diffusion times at higher positions. However, with the escalation of source energy and the involvement of a greater number of electrons, the height of the source no longer significantly affected reconstruction bias. Notably, as the electron count increased, the data points illustrating reconstruction bias began to align across different source heights. The investigation of initial interaction energy revealed a notable reduction from 0.45 mm to 0.1 mm in Δr for escalating electron counts from 1000 to 20000.

7.2 Outlook

The investigation conducted in this thesis opens up several paths for future research and development in the context of Xenoscope. Some key areas for further exploration include:

- **Enhanced Signal Simulation:** Expanding signal simulation capabilities by incorporating additional dependencies and considering intricate factors that affect signal behavior within the detector. This could involve accounting for more comprehensive physical processes and electron transport dynamics, such as updating the computation values for the diffusion process when new measurements are conducted.

- **Realistic Source Simulation using Geant4:** Moving towards a more realistic simulation framework by using Geant4 to generate simulated sources. Incorporating the geometry of the detector and accounting for energy attenuation considerations will provide a more precise representation of expected experimental data, facilitating improved calibration and analysis. This approach was started in previous works [50].

- **Advanced Position Reconstruction Algorithms:** Exploring advanced algorithms, particularly machine learning-based methods, for precise particle position reconstruction. Machine learning techniques hold promise in improving the accuracy and efficiency of position reconstruction, potentially reducing biases and uncertainties associated with this simplified approach [58].

- **Integration with DARWIN:** Extending the findings of this thesis to the DARWIN experiment and its dual-phase xenon TPC. Insights gained from studying the SiPM array in Xenoscope could directly optimize and enhance the performance of the larger-scale DARWIN detector.

The ongoing advancement of technology, simulation methodologies, and data analysis techniques holds the promise of enhancing precision and capabilities in future dark matter detection experiments, both within the Xenoscope detector and, in the longer term, within the DARWIN project.

8 Appendix

8.1 SiPM Waveforms

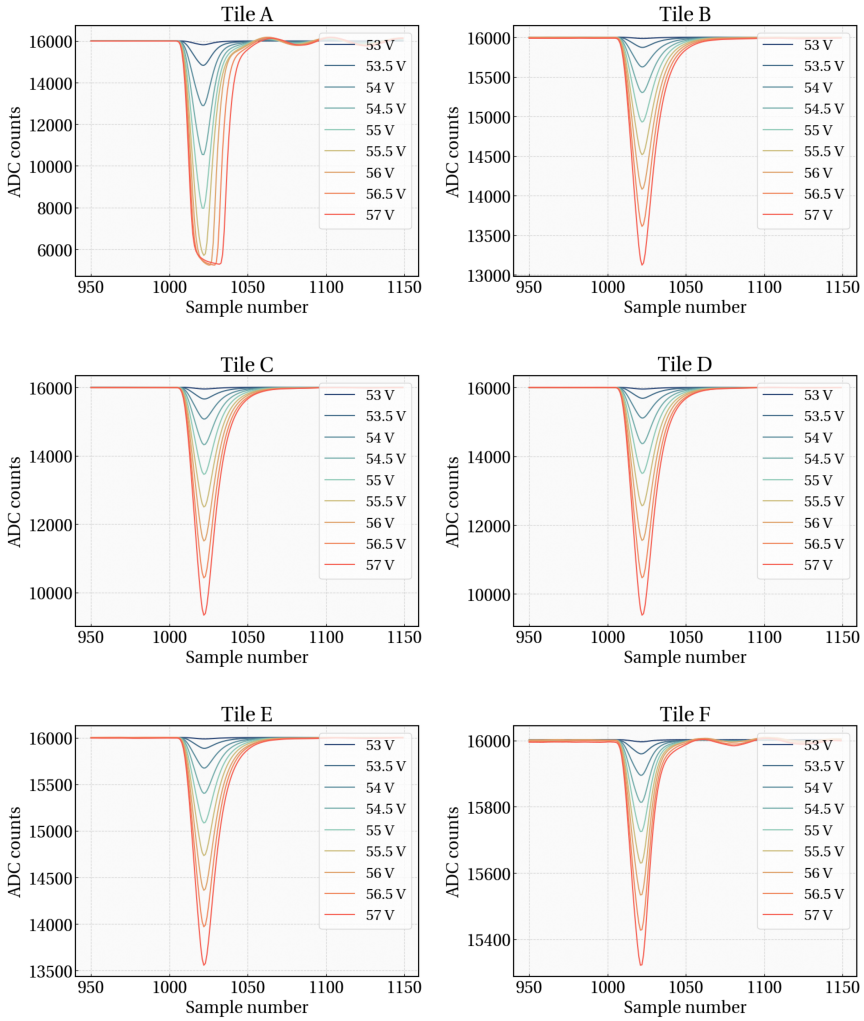

Figure 33: Waveforms obtained for different values of bias voltages.

8.2 Electron Extraction

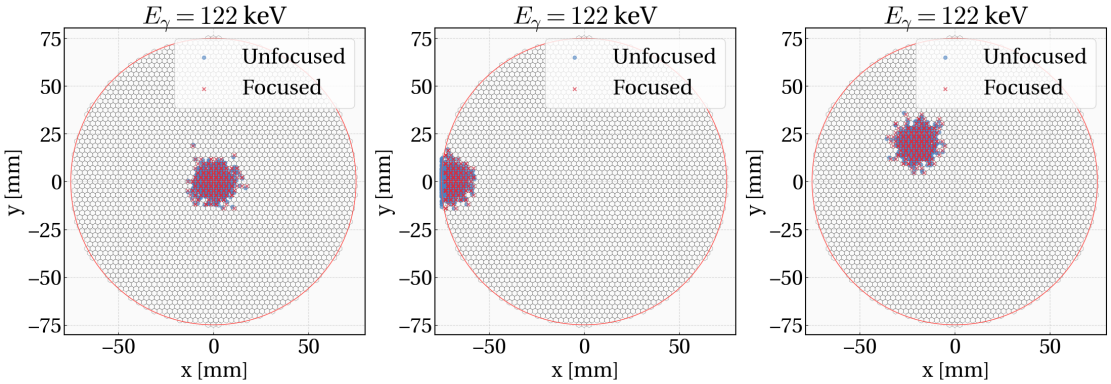

Figure 34: The interactions depicted in these figures occur at various initial positions: at the center of the TPC, along its edge, and at a position that lies between the SiPM photosensors.

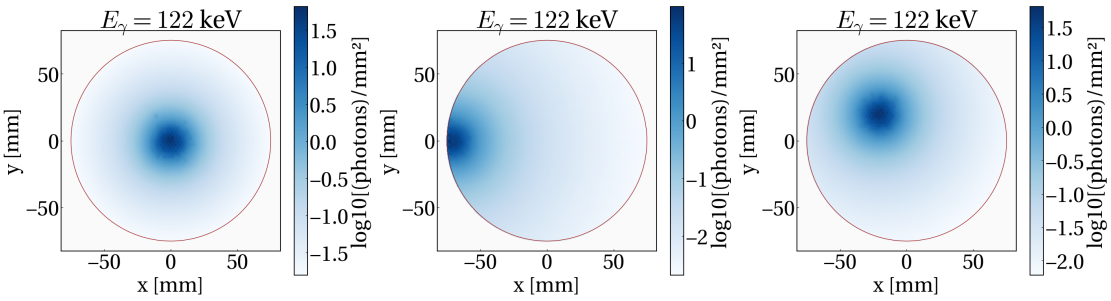

Figure 35: The light signals generated by extracted electrons from a $E_\gamma = 122$ keV gamma peak interaction are determined using the LCE maps.

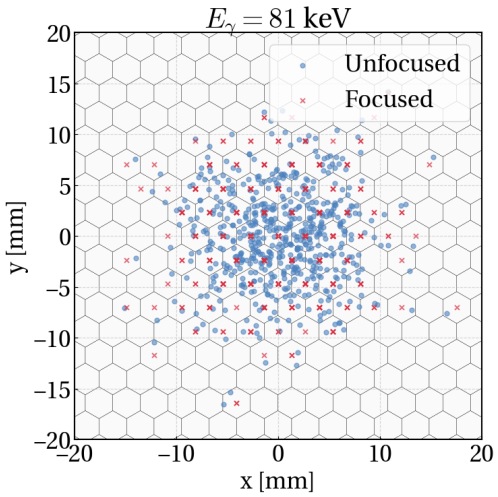

Figure 36: Zoomed in plot of extracted electrons.

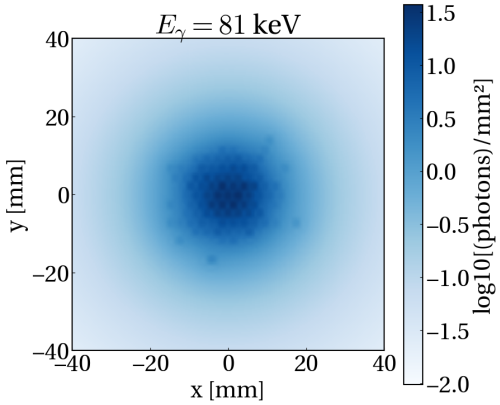

Figure 37: Zoomed in plot of simulated light signal.

8.3 Reconstruction Bias for Initial Position Mapping

The reconstruction maps are obtained for 1060 grid points, 50 iterations each. Using 10 CPU cores, the computation took around 30 hours.

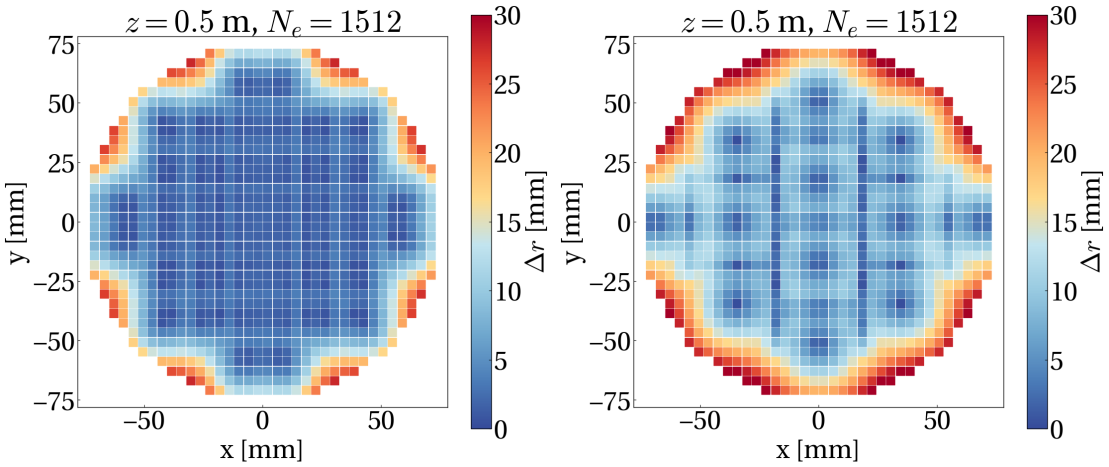

Figure 38: Position reconstruction bias maps.

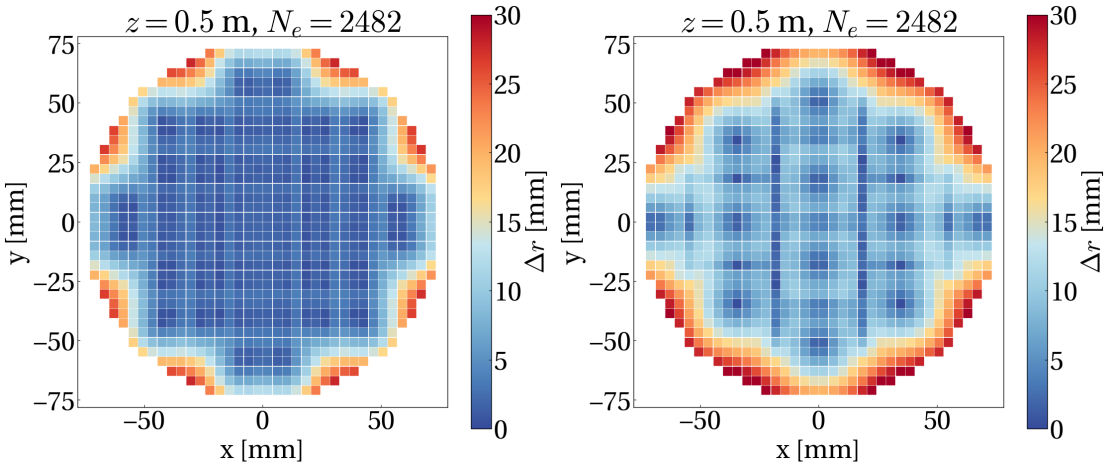

Figure 39: Position reconstruction bias maps.

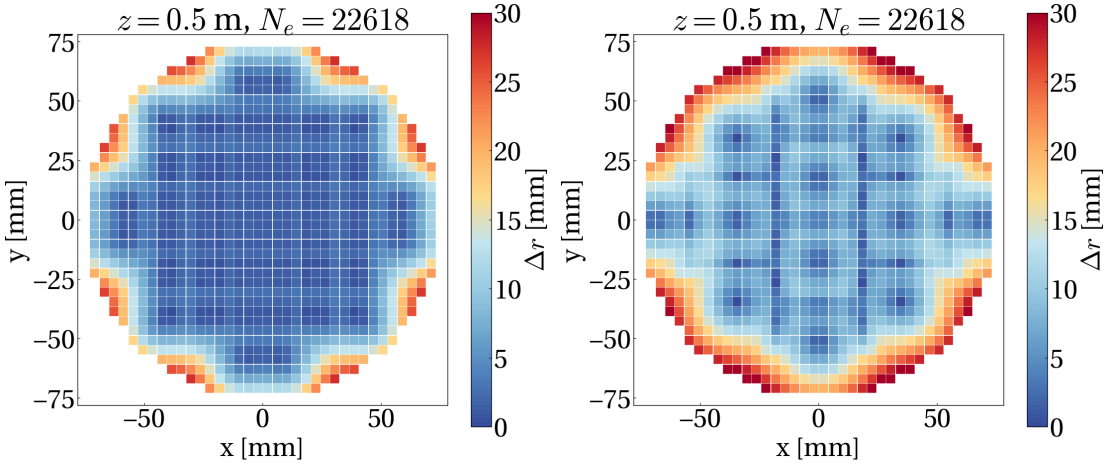

Figure 40: Position reconstruction bias maps.

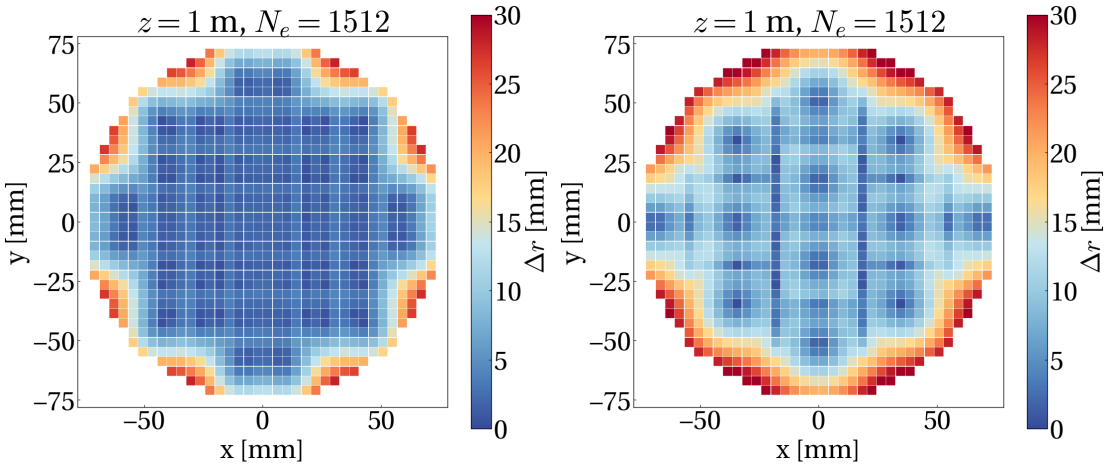

Figure 41: Position reconstruction bias maps.

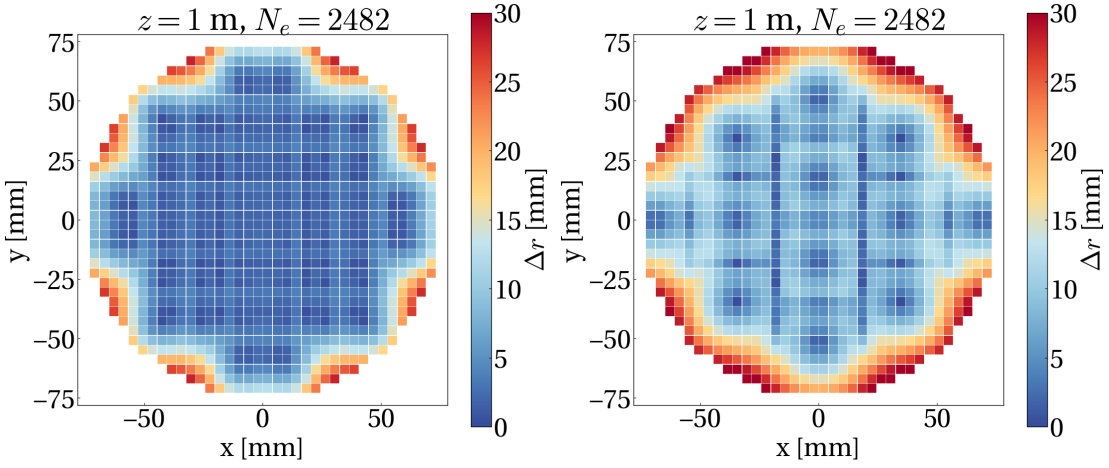

Figure 42: Position reconstruction bias maps.

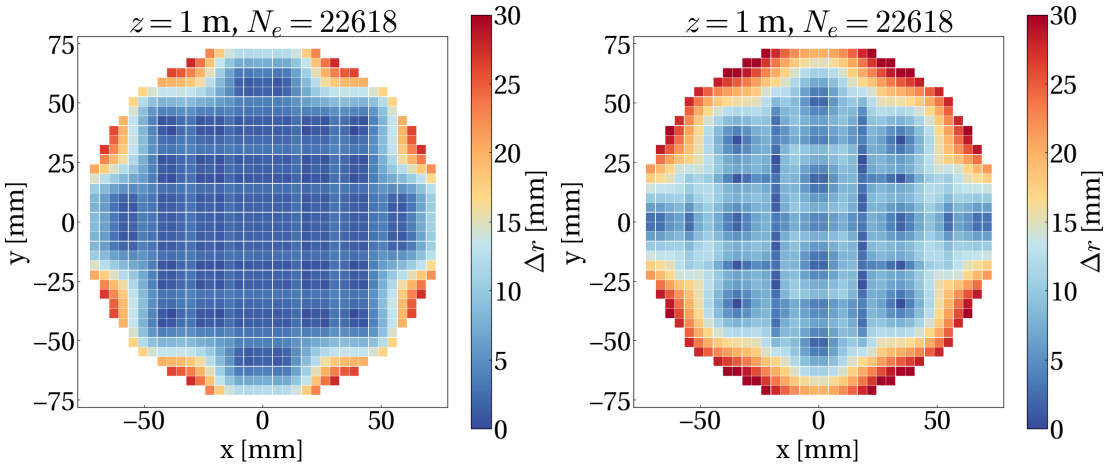

Figure 43: Position reconstruction bias maps.

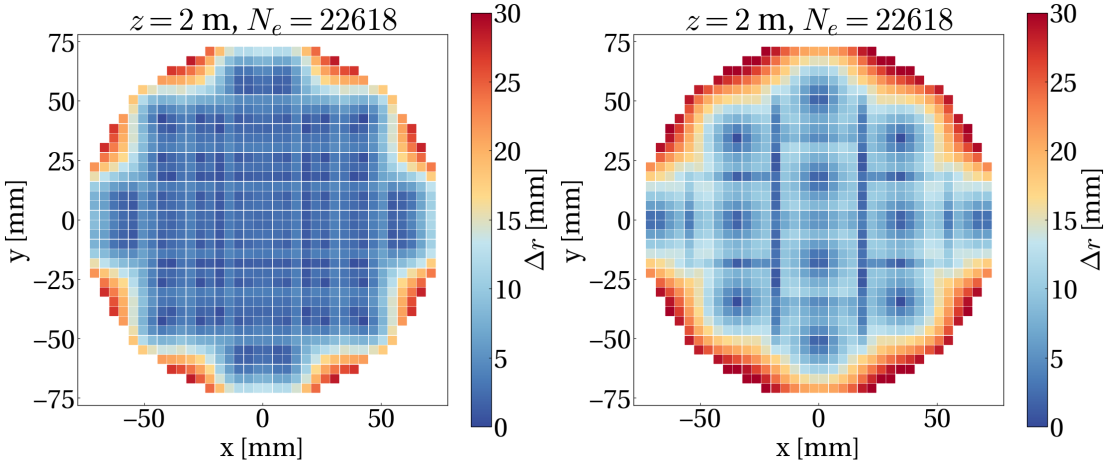

Figure 44: Position reconstruction bias maps.

Bibliography

[1] F. Zwicky. “Die Rotverschiebung von extragalaktischen Nebeln”. In: *Helv. Phys. Acta* 6 (1933), pp. 110–127. DOI: 10.1007/s10714-008-0707-4.

[2] and N. Aghanim et al. “iPlanck/i2018 results”. In: *Astronomy &amp Astrophysics* 641 (2020), A6. DOI: 10.1051/0004-6361/201833910. URL: https://doi.org/10.1051%2F0004-6361%2F201833910.

[3] J. Aalbers et al. “DARWIN: towards the ultimate dark matter detector”. In: *Journal of Cosmology and Astroparticle Physics* 2016.11 (2016), pp. 017–017. DOI: 10.1088/1475-7516/2016/11/017. URL: https://doi.org/10.1088%2F1475-7516%2F2016%2F11%2F017.

[4] L. Baudis et al. “Design and construction of Xenoscope — a full-scale vertical demonstrator for the DARWIN observatory”. In: *Journal of Instrumentation* 16.08 (2021), P08052. DOI: 10.1088/1748-0221/16/08/P08052. URL: https://dx.doi.org/10.1088/1748-0221/16/08/P08052.

[5] Anne Green. “Dark matter in astrophysics/cosmology”. In: *SciPost Physics Lecture Notes* (2022). DOI: 10.21468/scipostphyslectnotes.37. URL: https://doi.org/10.21468%2Fscipostphyslectnotes.37.

[6] II George W. Collins. *The Virial Theorem in Stellar Astrophysics*. Publisher, Year of Publication.

[7] Particle Data Group et al. “Review of Particle Physics”. In: *Progress of Theoretical and Experimental Physics* 2020.8 (Aug. 2020), p. 083C01. ISSN: 2050-3911. DOI: 10.1093/ptep/ptaa104. eprint: https://academic.oup.com/ptep/article-pdf/2020/8/083C01/34673722/ptaa104.pdf. URL: https://doi.org/10.1093/ptep/ptaa104.

[8] Vera C. Rubin and Jr. Ford W. Kent. “Rotation of the Andromeda Nebula from a Spectroscopic Survey of Emission Regions”. In: 159 (Feb. 1970), p. 379. DOI: 10.1086/150317.

[9] K. G. Begeman, A. H. Broeils, and R. H. Sanders. “Extended rotation curves of spiral galaxies: dark haloes and modified dynamics”. In: *Monthly Notices of the Royal Astronomical Society* 249.3 (Apr. 1991), pp. 523–537. ISSN: 0035-8711. DOI: 10.1093/mnras/249.3.523. eprint: https://academic.oup.com/mnras/article-pdf/249/3/523/18160929/mnras249-0523.pdf. URL: https://doi.org/10.1093/mnras/249.3.523.

[10] NASA. *Astronomy Picture of the Day*. 2017. URL: https://apod.nasa.gov/apod/ap170115.html.

[11] Douglas Clowe, Anthony Gonzalez, and Maxim Markevitch. "Weak-Lensing Mass Reconstruction of the Interacting Cluster 1E 0657–558: Direct Evidence for the Existence of Dark Matter*". In: *The Astrophysical Journal* 604.2 (2004), p. 596. DOI: 10.1086/381970. URL: https://dx.doi.org/10.1086/381970.

[12] Julien Billard et al. "Direct detection of dark matter—APPEC committee report∗". In: *Reports on Progress in Physics* 85.5 (2022), p. 056201. DOI: 10.1088/1361-6633/ac5754. URL: https://doi.org/10.1088%2F1361-6633%2Fac5754.

[13] Leszek Roszkowski, Enrico Maria Sessolo, and Sebastian Trojanowski. "WIMP dark matter candidates and searches—current status and future prospects". In: *Reports on Progress in Physics* 81.6 (2018), p. 066201. DOI: 10.1088/1361-6633/aab913. URL: https://doi.org/10.1088%2F1361-6633%2Faab913.

[14] Particle Data Group et al. "Review of Particle Physics". In: *Progress of Theoretical and Experimental Physics* 2022.8 (Aug. 2022), p. 083C01. ISSN: 2050-3911. DOI: 10.1093/ptep/ptac097. eprint: https://academic.oup.com/ptep/article-pdf/2022/8/083C01/49175539/ptac097.pdf. URL: https://doi.org/10.1093/ptep/ptac097.

[15] A. A. Penzias and R. W. Wilson. "A Measurement of Excess Antenna Temperature at 4080 Mc/s." In: 142 (July 1965), pp. 419–421. DOI: 10.1086/148307.

[16] Michael E. Peskin. "Supersymmetric dark matter in the harsh light of the Large Hadron Collider". In: *Proceedings of the National Academy of Sciences* 112.40 (2015), pp. 12256–12263. DOI: 10.1073/pnas.1308787111. eprint: https://www.pnas.org/doi/pdf/10.1073/pnas.1308787111. URL: https://www.pnas.org/doi/abs/10.1073/pnas.1308787111.

[17] Jonathan L. Feng. "The WIMP paradigm: Theme and variations". In: *SciPost Physics Lecture Notes* (2023). DOI: 10.21468/scipostphyslectnotes.71. URL: https://doi.org/10.21468%2Fscipostphyslectnotes.71.

[18] Gerard Jungman, Marc Kamionkowski, and Kim Griest. "Supersymmetric dark matter". In: *Physics Reports* 267.5 (1996), pp. 195–373. ISSN: 0370-1573. DOI: https://doi.org/10.1016/0370-1573(95)00058-5. URL: https://www.sciencedirect.com/science/article/pii/0370157395000585.

[19] Stefano Giagu. "WIMP Dark Matter Searches With the ATLAS Detector at the LHC". In: *Frontiers in Physics* 7 (2019). ISSN: 2296-424X. DOI: 10.3389/fphy.2019.00075. URL: https://www.frontiersin.org/articles/10.3389/fphy.2019.00075.

[20] Kevork N. Abazajian and J. Patrick Harding. "Constraints on WIMP and Sommerfeld-enhanced dark matter annihilation from HESS observations of the galactic center". In: *Journal of Cosmology and Astroparticle Physics* 2012.01 (2012), p. 041. DOI: 10.1088/1475-7516/2012/01/041. URL: https://dx.doi.org/10.1088/1475-7516/2012/01/041.

[21] V. A. Acciari et al. “VERITAS Search for VHE Gamma-ray Emission from Dwarf Spheroidal Galaxies”. In: 720.2 (Sept. 2010), pp. 1174–1180. DOI: 10.1088/0004-637X/720/2/1174. arXiv: 1006.5955 [astro-ph.CO].

[22] Aharonian, F. et al. “Probing the ATIC peak in the cosmic-ray electron spectrum with H.E.S.S.*”. In: *A&A* 508.2 (2009), pp. 561–564. DOI: 10.1051/0004-6361/200913323. URL: https://doi.org/10.1051/0004-6361/200913323.

[23] E. Aprile et al. “First Dark Matter Search with Nuclear Recoils from the XENONnT Experiment”. In: *Physical Review Letters* 131.4 (2023). DOI: 10.1103/physrevlett.131.041003. URL: https://doi.org/10.1103%2Fphysrevlett.131.041003.

[24] Ricardo José Mota Peres. “Advancing Multi-Messenger Astrophysics and Dark Matter Searches with XENONnT and the Top SiPM Array of Xenoscope”. PhD thesis. Zurich: University of Zurich, 2023.

[25] Frédéric Girard. “Design, Construction, and Operation of Xenoscope and Photosensor Characterisation for the DARWIN Observatory”. PhD thesis. Zurich: University of Zurich, 2023.

[26] Laura Baudis. *XeSAT 2023: Status and Outlook of XENON Experiments*. XeSAT 2023 Conference, Subatech, Nantes, June 7, 2023. https://indico.in2p3.fr/event/28661/contributions/125515/attachments/78259/114097/baudis_xesat2023.pdf. URL: https://indico.in2p3.fr/event/28661/contributions/125515/attachments/78259/114097/baudis_xesat2023.pdf.

[27] E. Aprile et al. “Projected WIMP sensitivity of the XENONnT dark matter experiment”. In: *Journal of Cosmology and Astroparticle Physics* 2020.11 (2020), pp. 031–031. DOI: 10.1088/1475-7516/2020/11/031. URL: https://doi.org/10.1088%2F1475-7516%2F2020%2F11%2F031.

[28] J. Aalbers et al. “First Dark Matter Search Results from the LUX-ZEPLIN (LZ) Experiment”. In: *Physical Review Letters* 131.4 (July 2023). ISSN: 1079-7114. DOI: 10.1103/physrevlett.131.041002. URL: http://dx.doi.org/10.1103/PhysRevLett.131.041002.

[29] X. G. Cao et al. *PandaX: A Liquid Xenon Dark Matter Experiment at CJPL*. 2014. arXiv: 1405.2882 [physics.ins-det].

[30] Chiara Capelli. “Search for Dark Matter and Neutrinoless Double Beta Decay in XENON1T and Calibration of the Photosensors in XENONnT”. PhD thesis. Universität Zürich, 2020.

[31] J. Wulf. “Direct Dark Matter Search with XENON1T and Developments for MultiTon Liquid Xenon Detectors”. PhD thesis. Universität Zürich, 2018.

[32] E. Aprile and T. Doke. “Liquid xenon detectors for particle physics and astrophysics”. In: *Rev. Mod. Phys.* 82 (3 2010), pp. 2053–2097. DOI: 10.1103/RevModPhys.82.2053. URL: https://link.aps.org/doi/10.1103/RevModPhys.82.2053.

[33] Carl Eric Dahl. "The physics of background discrimination in liquid xenon, and first results from Xenon10 in the hunt for WIMP dark matter". PhD thesis. Princeton U., 2009.

[34] Ricardo Peres. *PyLArS, comprhensive processing and analysis of SiPM data*. 2022. URL: https://github.com/ricmperes/PyLArS/.

[35] Laura Baudis et al. "A dual-phase xenon TPC for scintillation and ionisation yield measurements in liquid xenon". In: *The European Physical Journal C* 78.5 (2018). DOI: 10.1140/epjc/s10052-018-5801-5. URL: https://doi.org/10.1140%2Fepjc%2Fs10052-018-5801-5.

[36] F. Agostini et al. *Sensitivity of the DARWIN observatory to the neutrinoless double beta decay of ^{136}Xe*. 2020. arXiv: 2003.13407 [physics.ins-det].

[37] J. Aalbers et al. *Solar Neutrino Detection Sensitivity in DARWIN via Electron Scattering*. 2020. arXiv: 2006.03114 [physics.ins-det].

[38] Yanina Biondi. "Sensitivity of DARWIN to Rare Events and the Purity Monitor for Xenoscope". PhD thesis. Universität Zürich, 2022.

[39] L. Baudis et al. "The first dual-phase xenon TPC equipped with silicon photomultipliers and characterisation with $$^{37}\hbox {Ar}$$". In: *The European Physical Journal C* 80.5 (2020). DOI: 10.1140/epjc/s10052-020-8031-6. URL: https://doi.org/10.1140%2Fepjc%2Fs10052-020-8031-6.

[40] Yanina Biondi. "Purity monitor and TPC design for Xenoscope". In: *Journal of Physics: Conference Series* 2374.1 (2022), p. 012025. DOI: 10.1088/1742-6596/2374/1/012025. URL: https://dx.doi.org/10.1088/1742-6596/2374/1/012025.

[41] Narain Arora. "Review of Basic Semiconductor and pn Junction Theory". In: *MOSFET Models for VLSI Circuit Simulation: Theory and Practice*. Vienna: Springer Vienna, 1993, pp. 15–68. ISBN: 978-3-7091-9247-4. DOI: 10.1007/978-3-7091-9247-4_2. URL: https://doi.org/10.1007/978-3-7091-9247-4_2.

[42] Donald A. Neamen. *Semiconductor Physics and Devices: Basic Principles*. 2nd. Irwin, Chicago, 1997.

[43] Philip Hofmann. *Solid State Physics - An Introduction*. Wiley-VCH, 2008. ISBN: 978-3-527-40861-0.

[44] Brian Aull et al. "Three-dimensional imaging with arrays of Geiger-mode avalanche photodiodes". In: (Oct. 2005). DOI: 10.1117/12.633531.

[45] Fabio Acerbi and Sophie Gundacker. "Understanding and simulating SiPMs". In: *Nuclear Instruments and Methods in Physics Research Section A: Accelerators, Spectrometers, Detectors and Associated Equipment* 926 (2019).

[46] *Physics and Operation of the MPPC Silicon Photomultiplier*. Hamamatsu Photonics. URL: https://hub.hamamatsu.com/us/en/technical-notes/mppc-sipms/physics-and-operation-of-the-MPPC-silicon-photomultiplier.html.

[47] R. Peres. “SiPM array of Xenoscope, a full-scale DARWIN vertical demonstrator”. en. In: *Journal of Instrumentation* 18.03 (Mar. 2023), p. C03027. ISSN: 1748-0221. DOI: 10.1088/1748-0221/18/03/C03027. URL: https://iopscience.iop.org/article/10.1088/1748-0221/18/03/C03027 (visited on 05/03/2023).

[48] Hamamatsu Photonics K.K. *VUV4 MPPC B*. Hamamatsu Photonics K.K. 2017. URL: https://hamamatsu.su/files/uploads/pdf/3_mppc/s13370_vuv4-mppc_b_(1).pdf.

[49] *ricmperes/XenoDiffusionScope: Toy simulation of electrons in LXe for diffusion studies of Xenoscope*. URL: https://github.com/ricmperes/XenoDiffusionScope.

[50] Stefan Hochrein. “Background Measurement and MC Simulations for the DARWIN Demonstrator”. MA thesis. Zurich: University of Zurich, 2021.

[51] G. F. Knoll. *Radiation Detection and Measurement*. Ann Arbor: John Wiley & Sons, Inc., 1989. ISBN: 0-471-81504-7.

[52] *nest*. original-date: 2017-07-05T17:24:49Z. Apr. 2023. URL: https://github.com/NESTCollaboration/nest (visited on 05/02/2023).

[53] *Evaluated Nuclear Structure Data Files (ENSDF) database*. Accessed: 03.09.2021. URL: http://www.nndc.bnl.gov/ensarchivals/.

[54] L. Baudis et al. “The first dual-phase xenon TPC equipped with silicon photomultipliers and characterisation with ^{37}Ar”. In: *The European Physical Journal C* 80.5 (May 2020). arXiv:2003.01731 [astro-ph, physics:hep-ex, physics:nucl-ex, physics:physics], p. 477. ISSN: 1434-6044, 1434-6052. DOI: 10.1140/epjc/s10052-020-8031-6. URL: http://arxiv.org/abs/2003.01731 (visited on 05/02/2023).

[55] L. Baudis et al. *Electron transport measurements in liquid xenon with Xenoscope, a large-scale DARWIN demonstrator*. 2023. arXiv: 2303.13963 [physics.ins-det].

[56] E. Aprile et al. “XENON1T dark matter data analysis: Signal reconstruction, calibration, and event selection”. In: *Phys. Rev. D* 100 (5 2019), p. 052014. DOI: 10.1103/PhysRevD.100.052014. URL: https://link.aps.org/doi/10.1103/PhysRevD.100.052014.

[57] Alexander Bismark. *Simulationand CharacterizationofaLXe TPCforDARWINRD*. 2019.

[58] D.S. Akerib et al. “Position reconstruction in LUX”. In: *Journal of Instrumentation* 13.02 (2018), P02001. DOI: 10.1088/1748-0221/13/02/P02001. URL: https://dx.doi.org/10.1088/1748-0221/13/02/P02001.